Chemical Geology 506 (2019) 79–96

Contents lists available at ScienceDirect

Chemical Geology

journal homepage: www.elsevier.com/locate/chemgeo

Diagenetic mobilization of Ti and formation of brookite/anatase in early Cambrian black shales, South China

Ze-Rui Ray Liu[a], Mei-Fu Zhou[a,b,*], Anthony E. Williams-Jones[c], Wei Wang[d], Jian-Feng Gao[e]

[a] Department of Earth Sciences, the University of Hong Kong, Pokfulam Road, Hong Kong, China
[b] Faculty of Earth Resources, China University of Geosciences, Wuhan 430074, China
[c] Department of Earth and Planetary Sciences, McGill University, 3450 University Street, Montreal, QC H3A 0E8, Canada
[d] State Key Laboratory of Geological Processes and Mineral Resources, School of Earth Sciences, China University of Geosciences, Wuhan 430074, China
[e] State Key Laboratory of Ore Deposit Geochemistry, Institute of Geochemistry, Chinese Academy of Sciences, Guiyang 550081, China

ARTICLE INFO

Editor: K Johannesson

Keywords:
Brookite
Anatase
Ti mobility
Ti-mineralization
Black shales
South China

ABSTRACT

Titanium (Ti) is typically hosted in detrital minerals in marine sediments and has long been considered to be immobile during diagenesis. In this study, the authigenic titania minerals, brookite and anatase, are observed in early Cambrian carbonaceous shales from the Meishucun and Zhajin sections of South China, respectively. Black shales in the Meishucun section have total organic carbon (TOC) contents from 1.6 to 3.9 wt% and HI (hydrogen index) values from 3.8 to 20 mg HC/g TOC, whereas black shales in the Zhajin section have much higher TOC (7.1–15.6 wt%) but lower HI (< 2.0 mg HC/g TOC) and contain abundant bitumen (~3 vol%). Brookite in black shales from the Meishucun section crystallized invariably along cleavages of detrital biotite. This intimate association suggests that the Ti required to form titania minerals was derived from detrital biotite and that Ti was mobilized only on a nano- to micro-meter scale. In contrast, anatase aggregates in black shales from the Zhajin section are intergrown with bitumen. It is proposed that Ti in these shales was mobilized in low pH organic-rich fluids and, subsequently, preferentially precipitated as anatase with increasing pH. The mobilization of inert Ti in black shales is indicative of a possible diagenetic or post-diagenetic elemental redistribution in carbonaceous rocks. Our study further demonstrates that proxies based on geochemical component of black shales can be employed to estimate redox state of ancient oceans, but must be applied with caution.

1. Introduction

Authigenic titania minerals are rare in marine sediments due to the low concentration (0.005 to 0.35 nM) of Ti in seawater (Skrabal, 2006; Van Den Berg et al., 1994) and the inert behavior of detrital Ti-minerals (c.f. Cornu et al., 1999). Titanium is thus considered to be immobile in marine sediments and is thought to be a useful proxy in estimating the proportion of detrital components and sedimentary provenance (e.g., Young and Nesbitt, 1998; Wen et al., 2011). The notion of Ti immobility, however, has been challenged by recent observations that authigenic titania minerals are present in organic-rich sediments (e.g., Fuchs et al., 2015; Schulz et al., 2016). Indeed, it has been proposed that large amounts of Ti can be dissolved in organic carbon-rich waters/fluids (Parnell, 2004; Cabral et al., 2012), but sources of Ti and specific mechanisms of Ti-migration and precipitation remain unknown.

Authigenic titania minerals in organic-rich shales/siltstones consist dominantly of fine-grained brookite and anatase (Schulz et al., 2016), which display different growth habits from those formed by artificial synthesis. During syntheses of nano-crystalline TiO_2 solids, anatase is the first phase to crystallize due to its low surface energy, but it is typically replaced by a more stable phase, brookite, when the grain-size exceeds 11 nm (Zhang and Banfield, 2014). On heating to a temperature > 600 °C, both anatase and brookite are converted to rutile (Byrne et al., 2016), the only stable form of TiO_2 solids at all physico-chemical conditions encountered in the Earth's crust (Zhang and Banfield, 2014). In organic-rich shales/siltstones, however, TiO_2 is commonly present as anatase, which generally crystallizes within bitumen (Fuchs et al., 2015), or is found at oil-water contacts (Schulz et al., 2016); whereas the occurrence of brookite is restricted in sediments of lower thermal maturity (Schulz et al., 2016). Moreover, both brookite and anatase can grow to a micron-size without being transformed to rutile (Parnell, 2004; Fuchs et al., 2015).

Early Cambrian black shales are widely distributed on the southeastern margin of the Yangtze platform, South China (Guo et al., 2007;

* Corresponding author at: Department of Earth Sciences, the University of Hong Kong, Pokfulam Road, Hong Kong, China.
E-mail address: mfzhou@hku.hk (M.-F. Zhou).

https://doi.org/10.1016/j.chemgeo.2018.12.022
Received 29 August 2018; Received in revised form 18 December 2018; Accepted 19 December 2018
Available online 23 December 2018
0009-2541/

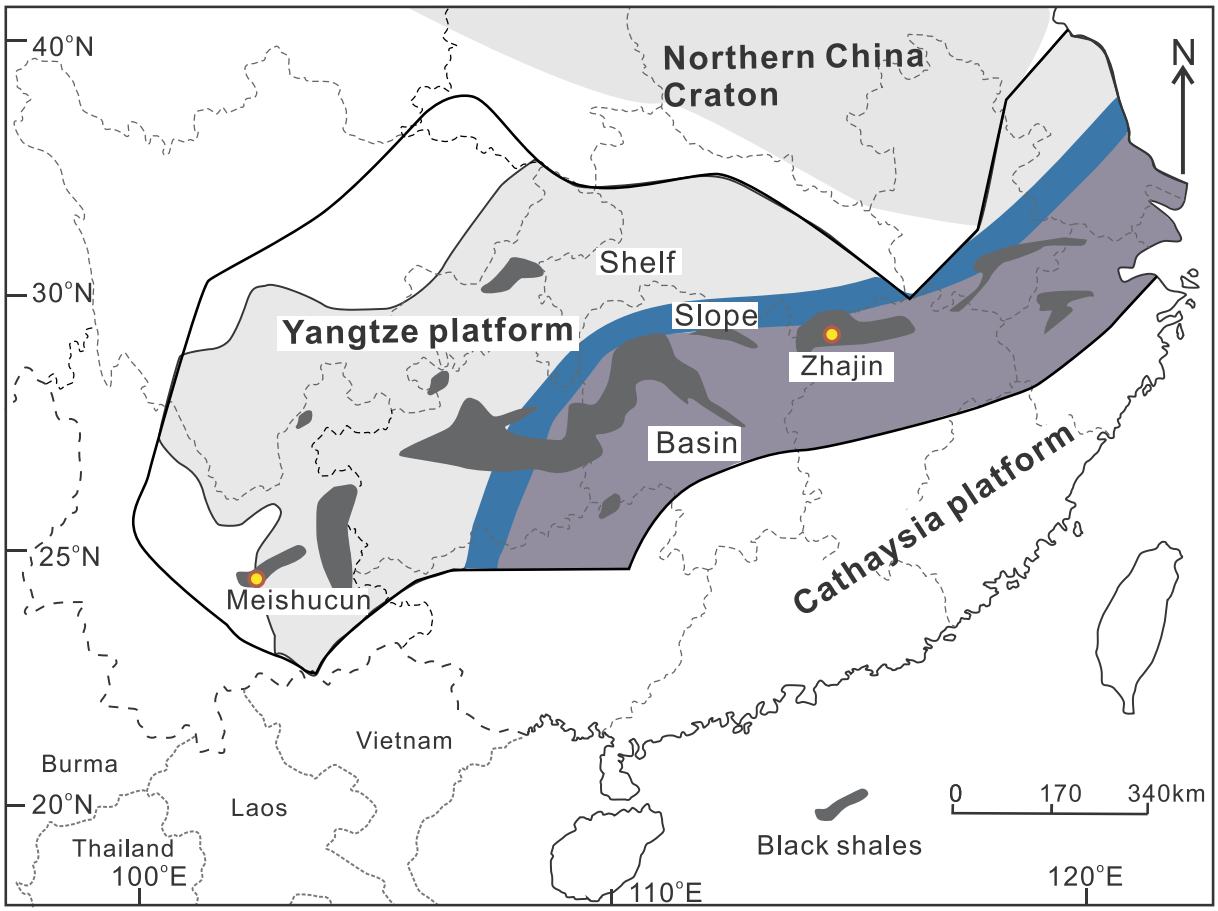

Fig. 1. Simplified paleogeographic map of the Yangtze platform during the Ediacaran-Cambrian transition, showing the three major facies under consideration (modified from Steiner et al. (2001); Zhang et al. (2017a)) Black areas indicate the exposed early Cambrian black shale sequence in South China (Xu et al., 2012).

Wen et al., 2015; Fig. 1). They formed under a variety of physico-chemical conditions due to variable contributions of continental and biotic components with increasing water and burial depth, and they have been shown to contain relatively high V concentrations (e.g., Bao et al., 2012; Jiang et al., 2006; Wen et al., 2015). In this paper, we report on authigenic Ti-bearing minerals from two early Cambrian black shale successions in South China. These black shales deposited on the continental shelf and slope-basin environments, respectively, and show contrasting morphologies and compositions. Results of this study provide new insights into the behavior of Ti in organic-rich sediments and a possible mechanism by which Ti can be mobilized and concentrated. We also discuss a possible re-distribution of redox sensitive elements in the black shales during their interaction with hydrocarbon liquids, and suggest that geochemical proxies for redox estimation should be used with caution.

2. Geological setting

Late-Neoproterozoic to early Cambrian sedimentary successions are well preserved in the Yangtze Block and were deposited in the paleo-environmental settings of a shelf, a protected basin and the transitional belt between them (Fig. 1). The earliest Cambrian rocks deposited in the basin, in order of increasing depths, are phosphorite/dolomite and black shale/chert. After a prolonged transgression, they are all overlain by a thick succession of black shales. Black shales in the Meishucun section (N 24° 43′ 19″ E 102° 33′ 24″), Yunnan province, and in the Zhajin section (N 28° 57′ 05″ E 114° 12′ 49″), Jiangxi province, were selected for this study (Figs. 1, 2a and 3a). Paleo-geographically, these two sections were located on a carbonate platform (Liu and Zhou, 2017; Wen et al., 2015) and in a transitional environment between the shelf and deep basin of the Yangtze platform, respectively (Fig. 1). Detailed descriptions of the regional geology are provided in Supplementary Note. Sixteen unaltered samples were collected from the Shiyantou Member in the Meishucun section and fourteen from the lower Wangyinpu Formation in the Zhajin section (see Supplementary Fig. S3). These two carbonaceous sedimentary sequences are stratigraphically correlative, and both were deposited during Cambrian Stage 1–2 (536 Ma–521 Ma) (see details in Supplementary material; Zhang et al., 2017b, Wen et al., 2015; Gao et al., 2018).

3. Analytical methods

3.1. Scanning electron microscopy

Scanning electron microscope (SEM) examination was carried out at the Henan Province Rock and Mineral Testing Center, China, using a ZEISS MERLIN Compact SEM equipped with an energy dispersive X-ray spectrometer (EDS), and back-scattered electron (BSE) detector. The Advanced Mineral Identification and Characterization System (AMICS) software package was used for the automated identification and quantification of minerals and synthetic phases. The acceleration voltage was 20 kV in BSE mode, which generated secondary electrons (SE_2) during imaging and EDS analyses. Based on petrographic observation under the SEM, the volume percent of major minerals, such as illite, quartz and biotite and titania were roughly estimated.

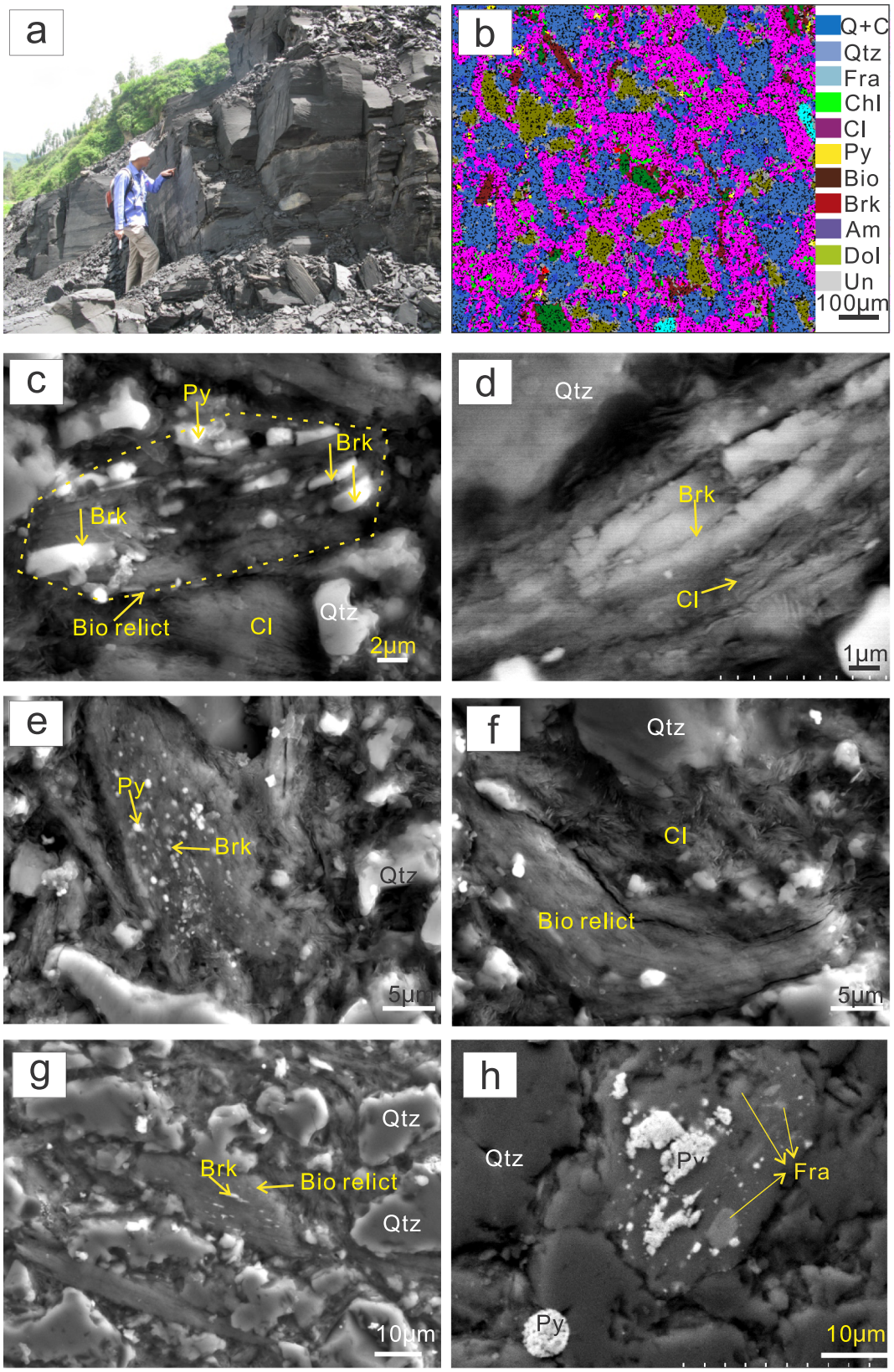

Fig. 2. Photograph (a), backscattered electron (BSE) (b and h) and secondary electron (SE_2) (c–g) images of the black shale in the Meishucun section. a) The black shale profile; b) mineral distribution in thin section oblique to the bedding plane using the AMICS software; c) tabular brookite crystals and pyrite along cleavages in a biotite relict; d) the biotite grains replaced by nano-crystalline aggregates of clay minerals; e) and f) authigenic clay minerals grown in the interstices between detrital grains; g) directional alignment of biotite; h) pyrite framboids and euhedral pyrite. Q + C = quartz + trace clay mineral; Qtz = quartz; Fra = Francolite; Chl = chlorite; Cl = clay minerals; Py = pyrite; Bio = biotite; Brk = brookite Am = amphibole; Dol = dolomite; Un = undermined mineral or holes or organic matter or bitumen.

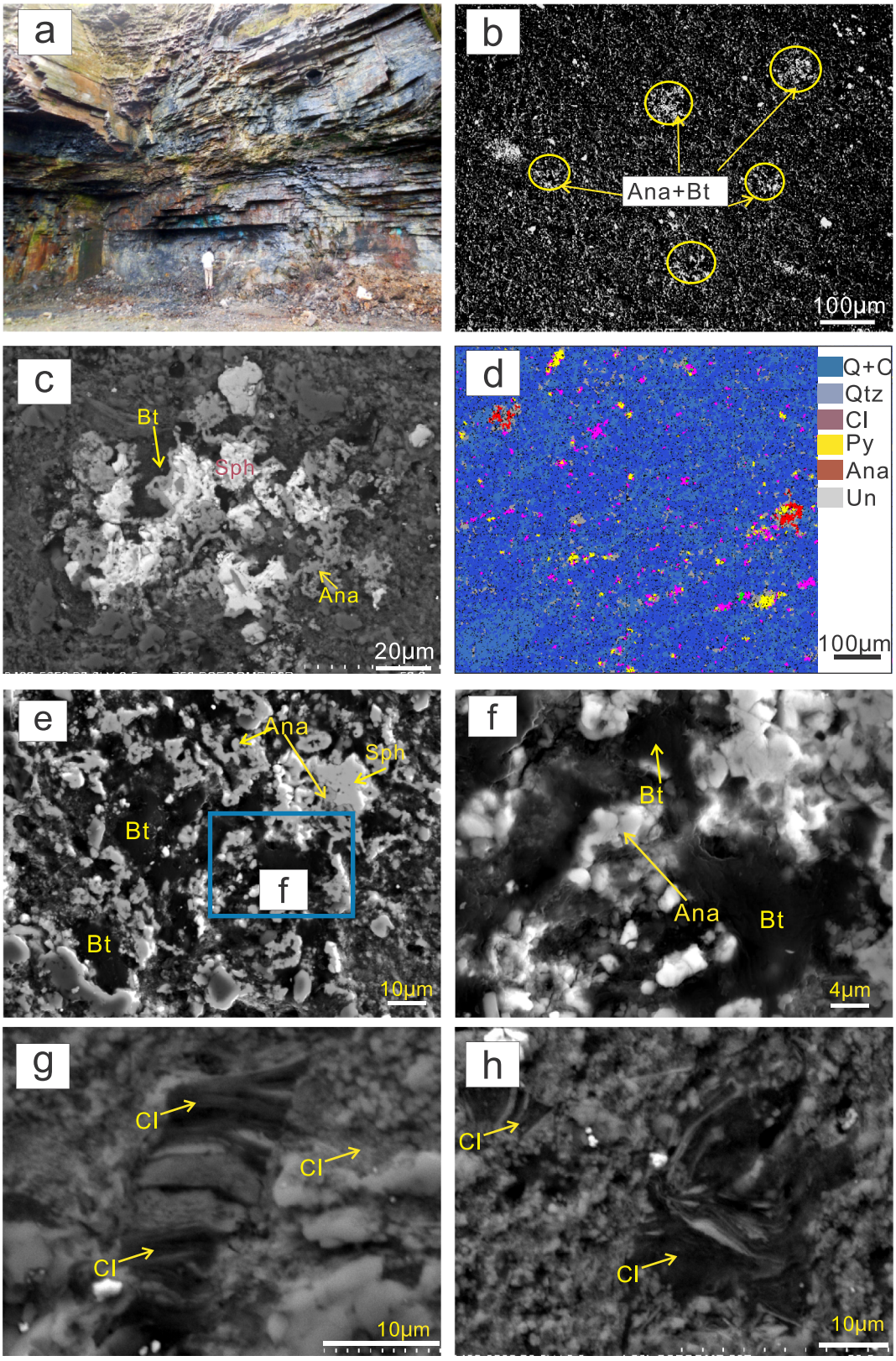

Fig. 3. Photograph (a), BSE (b–d, g and h) and SE_2 (e and f) images of black shales in the Zhajin section, Xiuwu area. a) black shales profile; b) disseminated anatase and bitumen; c) sponge-like anatase, and sphalerite intergrown with bitumen; d) mineral distribution determined using the AMICS software; anatase coated Fe-oxide; e) and f) the association of bitumen, sphalerite and anatase; g) and h) clay minerals. Ana = anatase; Un = undermined mineral or holes or organic matters; Bt = Bitumen.

3.2. Electron probe microanalysis

Major element compositions of minerals were obtained using a JXA-8230 electron microprobe at the University of Hong Kong. The quantitative analyses were performed in wavelength dispersive mode (WDS) with an accelerating voltage of 15 kV, a specimen current of 2.0×10^{-8} A, and a beam diameter of 1 μm. The analytical uncertainties were < 2%.

3.3. Laser Raman spectroscopy

Titania minerals were analyzed using a Thermo Scientific DXR dispersive Raman microscope equipped with an Olympus M plan-BD 100× objective at the State Key Laboratory of Geological Processes and Mineral Resources, China University of Geosciences (Wuhan). The analytical conditions are described in Xiong et al. (2011). A laser beam with an output power of 24 mW irradiated samples with a maximum power of 10 mW and an estimated spot size of 1 μm.

3.4. Transmission electron microscope (TEM)

Normally, samples for TEM imaging and analysis are mechanically polished to a thickness of a few micrometers and then milled to < 1 μm in thickness using a 4.0 kV argon ion-beam on a GATAN precise ion polishing system. However, black shales were too soft to be milled properly. In view of this, the samples were grounded to ~200 mesh and then, micron- and nano-size titania crystals for TEM analysis/imaging were selected using the SEM. The analyses were carried out at the Queen Mary Hospital, the University of Hong Kong, using a FEI Tecnai G2 20 S-TWIN scanning transmission electron microscope (dark field and bright field detectors with TIA acquisition software). The microscope is equipped with an INCAx-sight EDS Detector with INCA Energy TEM software, and Gatan image filtering system (749 1 k × 1 k camera system with digital/micrograph acquisition software).

3.5. Bulk rock trace element analyses

Samples analyzed in this study for their bulk composition were prepared by removing the surface rind with saw. They were then crushed with a steel jaw crusher, and powered using an aluminum oxide mill. Bulk rock concentrations of trace elements, including REEs, were determined using a VG Plasma-Quad Excell inductively coupled plasma mass spectrometer (ICP-MS) at the Institute of Geochemistry, Chinese Academy of Sciences (CAS), Guiyang, China, after a two-day closed-beaker digestion using a mixture of HF and HNO_3 acids in high-pressure autoclaves (Qi et al., 2000). Pure elemental standard solutions were used for external calibration and BHVO-1 and SY-4 were used as reference materials. The analyses were accurate to better than 5%.

3.6. Total organic carbon contents

Total organic carbon (TOC) contents were measured using a Multi EA 4000 carbon/sulfur analyzer with a high temperature furnace and acidification module (Eltra, Germany). Inorganic carbon (carbonate) was removed by adding 6 mol/L HCl to about 2 g of powdered shale. Approximately 100 mg of the solid residue was then weighed into a ceramic boat and combusted in pure (99.95%) O_2 at 1350 °C for ~3 min. The analytical errors for TOC were ± 0.2 wt% based on analysis of carbonate standard, AR4007 (Alpha, USA).

3.7. Rock-Eval pyrolysis

Rock-Eval pyrolysis experiments were performed on an OGE-VI Hydrocarbon Evaluation Work station at Yangtze University. Samples were progressively heated to 600 °C in a helium atmosphere. The measured parameters were S_1 (adsorbed free liquid hydrocarbons) which was measured in an oven at a constant temperature of 300 °C for 3 min; and S_2 (residual petroleum potential) which was measured when samples were heated from 300 to 600 °C at a rate of 25C/min. PRO-3 with S_1 = 0.61 mg HC/g rock and S_2 = 4.10 mg HC/g rock was used as standard material. The uncertainties for S_1 and S_2 were < ± 5% based on analysis of the standard. The HI parameter (hydrogen index) was calculated with following formula: $HI = 100 * S_2 / TOC$.

3.8. Sm–Nd isotopic analyses

Bulk rock Sm–Nd isotopic analyses were performed on a VG-354 thermal ionization magnetic sector mass spectrometer at the Institute of Geochemistry, Guiyang, China. The chemical separation and isotopic measurement procedures are described in Zhang et al. (2001). Mass fractionation corrections for Nd isotopic ratios were performed assuming a $^{146}Nd/^{144}Nd$ ratio of 0.7219. The uncertainty in the Sm/Nd isotopic ratio was less than ± 0.5% (relative).

4. Petrography

4.1. Black shales in the Meishucun section

Black shales in the Meishucun section are finely laminated, and composed of mineral assemblages, involving quartz aggregates, dolomite, pyrite, biotite, clay minerals and trace amphibole (Fig. 2b). Quartz, dolomite and clay minerals comprise > 80 vol% of the rocks (Fig. 2b). The quartz and dolomite grains are predominantly sub-angular to sub-rounded and range from 10 to 50 μm in diameter. There also contain minor proportions of biotite (3 vol%) and amphibole (< 0.5 vol%) crystals that are generally 10 μm in width and 20–100 μm in length (Fig. 2b–g). They are partially altered to chlorite (Fig. 2b–g). The clay minerals are < 2 μm in diameter, and occur in clusters in the interstices between quartz crystals or around biotite and amphibole crystals (Fig. 2e–g). Altered biotite crystals contain tabular brookite crystals (see below for how they were identified) and euhedral pyrite grains along their cleavages (Fig. 2c–g). Without exception, the brookite is restricted to biotite relicts, whereas pyrite is much more prevalent in the matrix, where it occurs as euhedral crystals, framboids or nodular aggregates, and generally ranges from 2 to 15 μm in diameter (Fig. 2h). Authigenic phosphatic grains (colloidal nodules) are sparsely distributed and occupy < 2 vol% of the rock (Fig. 2b).

4.2. Black shales in the Zhajin section

Black shales in the Zhajin section are variably layered, and in places display distinct submillimeter-scale parallel laminae or thin-thick beds (Fig. 3a). They are composed mainly of quartz, clay minerals, titania minerals, pyrite and bitumen (Figs. 3 and 4). Quartz and clay minerals, comprising > 80 vol% of the rock, are typically < 5 μm in diameter (Fig. 4). Disseminated anatase (see below for methods of identification) comprises up to 3 vol% of the rock and occurs as sponge-like aggregates of micron-size crystals (Fig. 3b–f). These aggregates commonly crystallized around sphalerite and range from 50 μm to 300 μm in diameter (Fig. 3c–f). Sphalerite is amorphous and porous. Bitumen (~3 vol%) is disseminated throughout the rock; it occupies interstices among sphalerite and titania mineral aggregates (Figs. 3 and 4). Authigenic quartz and clay minerals are enclosed in bitumen (Fig. 4c and d). The clay mineral crystals are sheet-like and < 2 μm in diameter, and aggregating in the interstices among the quartz crystals (Fig. 3g and h). Pyrite occurs as framboids, euhedral crystals or pseudomorphs replacing animal fossils.

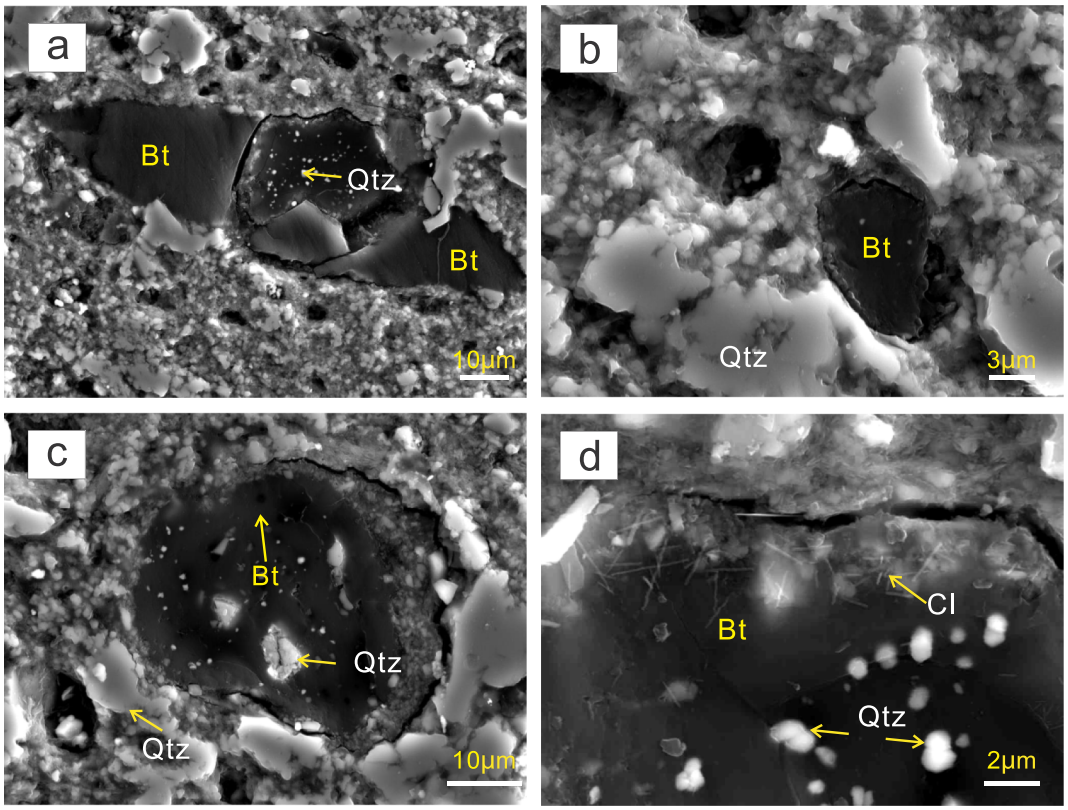

Fig. 4. Secondary electron (a–d) and BSE (e and f) images of the black shale in the Zhajin section, Xiuwu area. a) and b) Bitumen filling pores in the black shales; c) quartz fragments in bitumen; d) clay mineral in contact with bitumen.

5. Chemical composition of crystalline and organic phases

5.1. Brookite/anatase

Titania minerals in biotite relics of black shales from the Meishucun section produced a sharp peak at ~153 cm^{-1} and low-intensity peaks at 127, 213, 247, 284, 327, 369, 456 and 544 cm^{-1} on the Raman spectrum (Fig. 5a). These peaks correspond to those for brookite in a direction parallel to XX (the 127, 153, 247 and 544 cm^{-1} peaks), XY (the 213, 284 and 327 cm^{-1} peaks) and XZ (the 369 and 456 cm^{-1} peaks (Fig. 5a; Iliev et al., 2013). All titania crystals in black shales from the Zhajin section produced strong peaks at about 146, 396, 513 and 635 cm^{-1}. These wave numbers are diagnostic of anatase (Fig. 5a; Frank et al., 2012). Transmitted electron microscopic analysis of titania crystals from black shales of the Zhajin section yielded an electron diffraction pattern for the $[\bar{1}, 1, \bar{1}]$ plane, corresponding to d-spacings of 0.3595 nm (1,0, $\bar{1}1$) and 0.3609 nm (0,1, $\bar{1}$) (Fig. 5b–d). These d-spacings, within the experimental error, are the same as those for the $[\bar{1}, \bar{1}, \bar{1}]$ plane of anatase (0.3516 nm) and confirm the Laser Raman Spectroscopic identification (Fig. 5).

In order to further characterize the titania minerals, their chemical compositions were determined using the electron microprobe (EMP). The EMP analytical data were obtained from a spot with a diameter of 1 μm that correspond to an excitation volume with a diameter of ~4 μm, which is larger than most of the analyzed mineral grains. Therefore, the EMP data represent an average composition of numerous individual nano-size crystals and possibly also non-titania mineral components. The valances of Fe and V in the minerals were not determined and instead are reported as FeO and V_2O_3 contents. Brookite from the black shales of the Meishucun section has elevated Al_2O_3 (0.43–3.9 wt%), SiO_2 (0.95–10 wt%) and FeO (0.74–3.6 wt%) contents, which may reflect contamination from the surrounding clay minerals, and relatively low V_2O_3 (0.23–1.93 wt%) and TiO_2 (71–91 wt%) contents. By contrast, anatase from the black shales of the Zhajin section has high SiO_2 (0.36–5.3 wt%) and low Al_2O_3 (0.1–1.0 wt%) contents, suggesting that the contamination was mainly from quartz that filled interstices within the anatase aggregates. The anatase has a FeO content from 0.47 to 1.4 wt%, a V_2O_3 content from 3.4 to 5.4 wt% and a TiO_2 content from 75 to 93 wt% (Fig. 6; Table 1).

5.2. Phyllosilicate minerals

Biotite crystals in the black shales from the Meishucun section have low SiO_2 contents, ranging from 30 wt% to 36.2 wt%, and high FeO (17–20 wt%) and TiO_2 (> 0.23 wt%) contents, whereas the clay minerals have high SiO_2 (45–57 wt%) and Al^{VI} (2.4–3.9 atoms per formula unit) contents (Fig. 7a and b). The small clay mineral crystals are compositionally similar to the large muscovite crystals (Table 2). They have relatively high Fe/Fe + Al ratios and moderate K contents, consistent with Al-rich mixed layer illite-smectite (I/S), smectite or Fe-rich I/S (Fig. 7b). All the clay minerals in the black shales of the Meishucun section have low V_2O_3 (< 0.2 wt%) and Cr_2O_3 (< 0.14) contents.

Clay minerals in the black shales of the Zhajin section have low Fe/Fe + Al ratios and variable K contents, indicating that they comprise kaolinite, Al-rich I/S and illite (Fig. 7b). Vanadium is negatively correlated with Al^{VI} in the clays (Fig. 7c). Most of the clay minerals have high V_2O_3 (ca. 2.5 wt%) and low TiO_2 (0.22 wt%) contents; V_2O_3 and TiO_2 contents display a positive correlation, except for minerals with a very low V_2O_3 content (Fig. 7d).

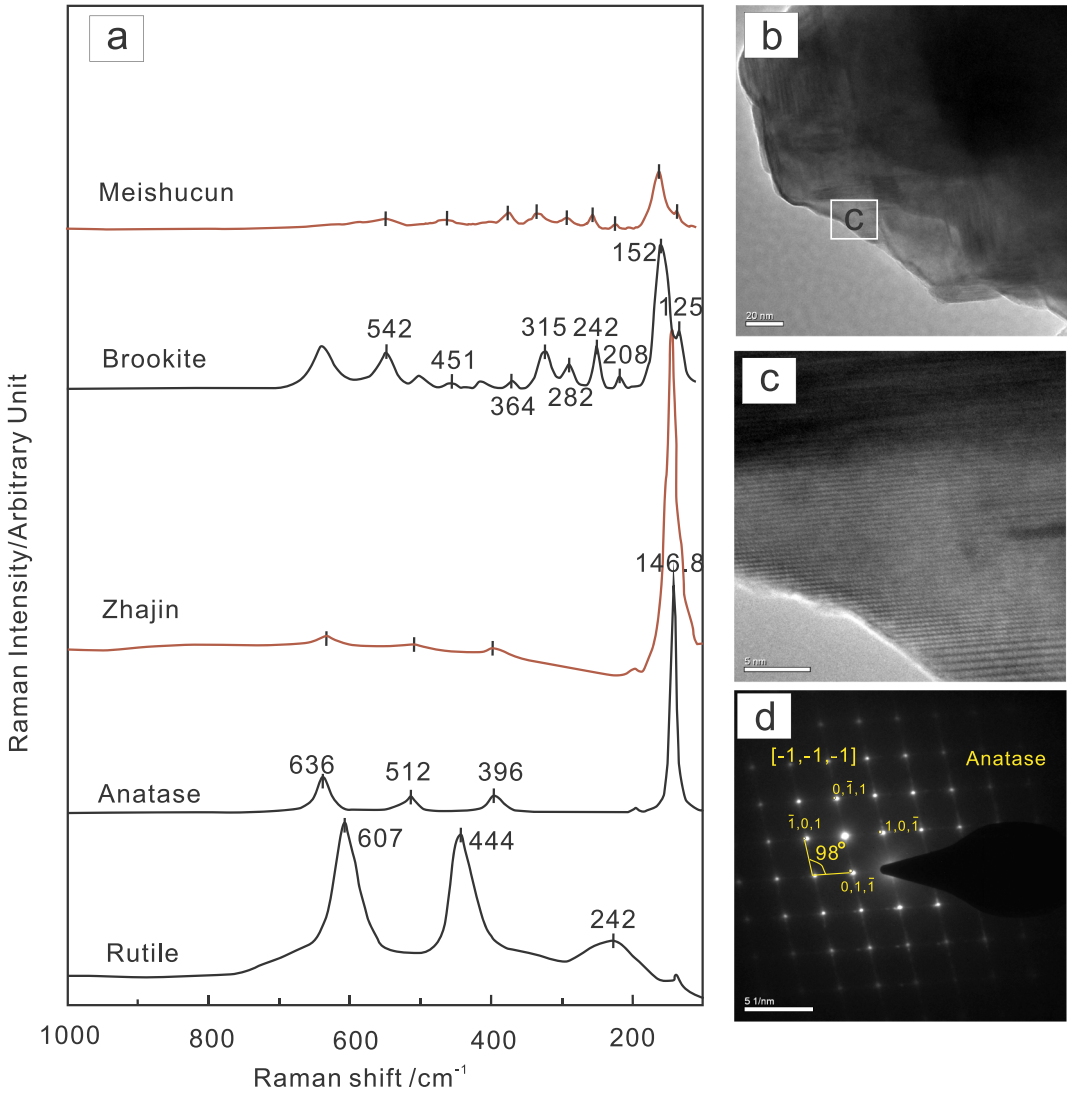

Fig. 5. Raman shift and a TEM image of titania minerals from black shales of the Meishucun and Zhajin sections, South China. a) Raman shift diagram, the red lines illustrate our spectra and the black line the spectra presented in (Iliev et al., 2013); b) bright field TEM images of anatase crystals from the Zhajin section; c) enlargement of the area labeled "c" in (b), showing individual anatase crystals; d) electron diffraction pattern for the $[\bar{1}, \bar{1}, 1]$ plane of anatase.

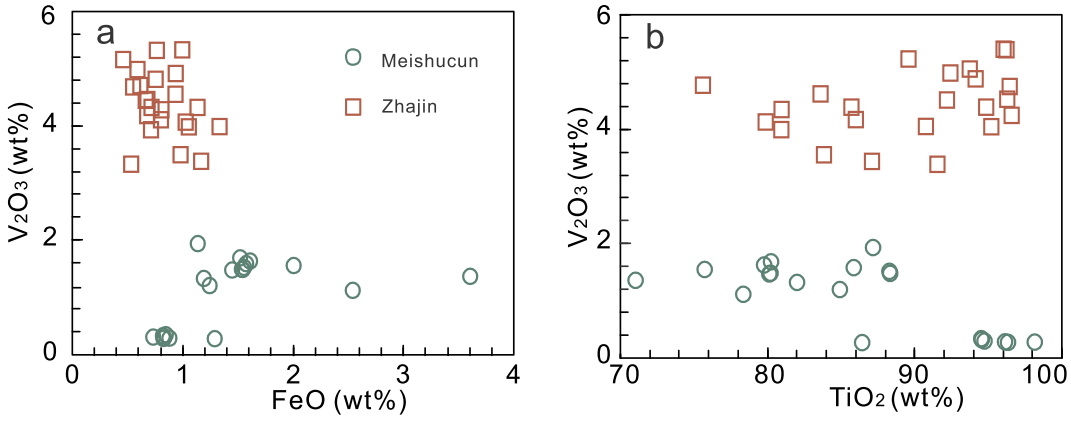

Fig. 6. Binary diagrams illustrating compositional data for the titania minerals.

Table 1
Major elemental compositions of titania in black shales from the Meishucun and Zhajin sections, South China.

Location	Meishucun section														
Sample no.	B9-2-5	B9-2-6	B9-2-7	B9-2-8	B9-2-9	B9-2-10	B9-8-5	B9-8-6	B9-8-7	B9-8-8	B9-8-9	B9-8-10	B9-16-3	B9-16-4	B9-16-5
Description	Brookite	Brookite	Brookite	Brookite	Brookite	Brookite	Brookite	Brookite	Brookite	Brookite	Brookite	Brookite	Brookite	Brookite	Brookite
SiO_2	5.2	5.24	4.06	6.57	7.94	6.67	3.86	2.33	2.52	3.13	10.33	5.18	0.95	0.99	3.92
TiO_2	82	80.3	87.2	80.2	75.7	79.7	85.8	88.3	88.3	80.1	71	78.3	96.3	98.1	86.4
Al_2O_3	2.87	2.97	2.44	3.91	2.58	3.43	1.63	0.92	1	1.49	3.41	3.05	0.43	0.52	2.41
Cr_2O_3	0.52	0.61	0.26	0.3	0.33	0.27	0.14	0.11	0.1	0.16	0.16	0.26	0.01	0.01	0.02
V_2O_3	1.32	1.4	1.93	1.68	1.55	1.62	1.58	1.52	1.48	1.47	1.35	1.11	0.27	0.28	0.27
FeO	1.2	1.23	1.15	1.53	2.02	1.62	1.59	1.57	1.55	1.46	3.62	2.55	0.83	0.89	1.3
MnO	0.04	0.03	0	0.02	0.01	0	0	0.04	0	0	0.04	0.02	0	0.01	0
MgO	1.29	1.12	0.97	1.92	2.66	2.61	1.64	0.92	1.02	1.19	5.04	1.52	0.25	0.26	0.99
CaO	0.14	0.23	0.11	1.13	0.3	0.65	0.48	1.25	1.31	4.28	0.39	2.08	0.32	0.31	0.33
BaO	0.49	0.52	0.47	0.48	0.47	0.49	0.53	0.52	0.58	0.5	0.46	0.44	0	0	
Na_2O	0.14	0.18	0.13	0.16	0.14	0.14	0.07	0.05	0.04	0.19	0.09	0.12	0.04	0.01	0.01
K_2O	0.73	0.65	0.71	0.98	0.84	0.75	0.43	0.31	0.32	0.38	0.94	0.79	0.19	0.22	0.7
Total	95.9	94.5	99.4	98.9	94.5	98	97.8	97.8	98.2	94.3	96.8	95.4	99.6	101.6	96.4

Location	Meishucun section						Zhajin section								
Sample no.	B9-16-6	B9-16-7	B9-16-8	B9-16-9	B9-16-10	B9-16-11	JX37-1-7	JX37-1-8	JX37-1-9	JX37-1-10	JX37-13-16	JX37-13-17	JX37-13-18	JX37-13-19	JX37-13-20
Description	Brookite	Brookite	Brookite	Brookite	Brookite	Brookite	Anatase	Anatase	Anatase	Anatase	Anatase	Anatase	Anatase	Anatase	Anatase
SiO_2	1.58	0.99	1.59	3.8	2.06	4.91	1.77	0.85	1.13	1	1.61	3.16	5.32	1.54	1.64
TiO_2	94.5	96.1	94.5	84.9	94.7	80.2	83.3	83.1	86.3	88	89.8	81.3	79.1	74.7	87.3
Al_2O_3	0.47	0.52	0.46	2	1.33	2.59	0.36	0.49	0.39	0.27	0.46	0.72	0.56	1	0.32
Cr_2O_3	0.04	0.03	0.02	0.56	0.09	0.45	0.16	0.22	0.27	0.18	0.18	0.2	0.17	0.22	0.19
V_2O_3	0.31	0.28	0.33	1.19	0.29	1.48	4.14	4.36	5.2	3.36	5.03	4.59	3.97	4.75	4.02
FeO	0.83	0.84	0.86	1.26	0.74	1.55	0.81	1.14	0.47	0.54	0.6	0.94	0.72	0.62	1.34
MnO	0.02	0	0.01	0.02	0	0.01	0	0.01	0	0	0.02	0	0	0	0
MgO	0.29	0.33	0.3	0.97	0.56	1.29	0.02	0.02	0.02	0	0.03	0.03	0.03	0.1	0.03
CaO	0.34	0.28	0.32	0.42	0.28	0.58	0.1	0.15	0.03	0.11	0.13	0.21	0.14	0.06	0.16
BaO							0.39	0.44	0.47	0.52	0.51	0.49	0.46	0.44	0.49
Na_2O	0.03	0.02	0.02	0.02	0.01	0.09	0.1	0.09	0.03	0.31	0.03	0	0.05	0.03	0.01
K_2O	0.2	0.21	0.2	0.55	0.47	0.66	0.02	0	0.05	0.03	0.04	0.01	0.04	0.12	0.01
Total	98.6	99.6	98.6	95.7	100.6	93.8	91.2	90.9	94.4	94.3	98.4	91.7	90.6	83.6	95.5

Location	Zhajin section													
Sample no.	JX37-13-21	JX37-13-22	JX37-13-23	JX37-23-8	JX37-23-9	JX37-23-10	JX37-23-11	JX37-23-12	JX37-23-13	JX37-23-14	JX37-23-15	JX37-23-16	JX37-23-17	JX37-23-18
Description	Anatase	Anatase	Anatase	Anatase	Anatase	Anatase	Anatase	Anatase	Anatase	Anatase	Anatase	Anatase	Anatase	Anatase
SiO_2	9.88	0.4	1.09	2.04	0.36	0.6	0.69	0.52	1.08	2.65	3.27	2.18	0.73	0.53
TiO_2	78.2	88.7	91.9	92.1	91.9	92.2	90.7	91.7	90.1	84.3	81.6	79.1	91	88.5
Al_2O_3	0.44	0.47	0.36	0.24	0.32	0.21	0.16	0.11	0.15	0.16	0.24	0.11	0.26	0.25
Cr_2O_3	0.18	0.21	0.21	0.24	0.23	0.28	0.25	0.25	0.22	0.3	0.27	0.27	0.21	0.22
V_2O_3	4.1	4.96	4.5	4.72	5.36	4.22	4.36	5.37	4.86	3.41	3.53	4.32	4.02	4.49
FeO	1.03	0.94	0.69	0.56	0.77	0.68	0.72	1	0.76	1.17	0.99	0.81	1.06	0.67
MnO	0	0	0.02	0	0.01	0	0.04	0	0.02	0.01	0.01	0	0	0

(*continued on next page*)

Table 1 (*continued*)

Location	Zhajin section													
Sample no.	JX37-13-21	JX37-13-22	JX37-13-23	JX37-23-8	JX37-23-9	JX37-23-10	JX37-23-11	JX37-23-12	JX37-23-13	JX37-23-14	JX37-23-15	JX37-23-16	JX37-23-17	JX37-23-18
Description	Anatase	Anatase	Anatase	Anatase	Anatase	Anatase	Anatase	Anatase	Anatase	Anatase	Anatase	Anatase	Anatase	Anatase
MgO	0.03	0.01	0.01	0.02	0.02	0.01	0.01	0	0	0.02	0.03	0.05	0.02	0.03
CaO	0.12	0.11	0.11	0.09	0.11	0.09	0.1	0.12	0.08	0.1	0.13	0.14	0.13	0.14
BaO	0.46	0.5	0.51	0.51	0.53	0.53	0.57	0.54	0.57	0.51	0.47	0.47	0.53	0.54
Na_2O	0.01	0	0.01	0.01	0	0.01	0	0.01	0.03	0	0.02	0.01	0.01	0.01
K_2O	0.03	0.01	0.02	0.02	0.01	0.01	0.01	0	0	0	0.02	0.05	0	0.02
Total	94.5	96.3	99.5	100.5	99.6	98.8	97.6	99.7	97.9	92.6	90.5	87.6	98	95.4

5.3. Organic phases

Forty energy dispersive X-ray spectroscopic and 14 EPM spot analyses of the bitumen aggregates in black shales from the Zhajin section yielded large peaks for carbon and oxygen and small peaks for Si, Al, S, K, Ti, V, Fe and Zn (Table 3 and Supplementary Table A1). Black shales of the Meishucun section have much lower TOC contents (1 to 4 wt%) than those of the Zhajin section (7 to 15 wt%) (Table 4; Fig. 8). However, they have higher S_1 (0.04–0.24 mg HC/g rock), S_2 (0.1–0.43 mg HC/g rock) and HI (3.8–20 mg HC/g TOC) values than black shales of the Zhajin section with S_1 = 0.01–0.14 mg HC/g rock, S_2 = 0.01–0.29 mg HC/g rock and HI = 0.1–2.0 mg HC/g TOC (Table 4).

6. Bulk rock compositions

Black shales from the Meishucun section have high Ti (5205 ppm on average) and low V (98–555 ppm) contents. They also have high Sc (13.8–17.4 ppm), Co (9.8–17.5 ppm) and Th (5.9–11 ppm) contents and low Cr (60–781 ppm), Ni (39–86 ppm) and U (4.4–15.8 ppm) contents. By comparison, black shales in the Zhajin section have over an order of magnitude higher V (2900–11,000 ppm), and much higher Cr (125–1221 ppm), Ni (41–294 ppm) and U (28–663 ppm) contents than black shales from the Meishucun section. However, they have significantly lower Ti (1830 ppm on average), Sc (4–16 ppm), Co (0.4–15.4 ppm) and Th (3.1–6.5 ppm) contents. Barium is highly enriched in Ba-feldspar-rich layers in black shales from the Zhajin section. Black shales from both sections have negative εNd(t) (t = 525 Ma) values (−6.91 to −5.74; Table 5), although a relatively higher εNd(t) value (0.49) was obtained for a shale sample at the top of the Zhajin section.

7. Discussion

7.1. Derivation of Ti from detrital components

Detrital titania minerals are rarely observed in marine sediments owing to their high density (3.8–4.3 g/cm^3) which impedes their transport into marine basins (Schulz et al., 2016). Wherever these minerals are present, they are either rounded in shape (Baioumy, 2014) or show signs of partial dissolution (Schulz et al., 2016). In contrast, brookite in black shales of the Meishucun section occurs as tabular crystals along cleavages of biotite (Fig. 2c), and anatase in black shales of the Zhajin section forms sponge-like crystal aggregates and intergrow with sphalerite (Fig. 3c). These observations imply that the titania minerals (brookite and anatase) in the Meishucun and Zhajin black shales are authigenic in origin.

Vertical redox changes and remineralization of organic matter in the water column are two widely invoked mechanisms for producing trace element-rich authigenic minerals in sediments (Algeo and Maynard, 2004; Emerson and Huested, 1991; Gregory et al., 2017; Jones and Manning, 1994). During the deposition of black shales, accumulation and subsequent decay of organisms along and below the water-sediment interface consumes the O_2 of the bottom water, generating a stratified redox state in the basin (Kristensen, 2000). Redox sensitive elements, such as V, Mo and Cr, have relatively high solubility under oxic conditions and are insoluble in reduced environments. They are thus precipitated and accumulated in black shales (Algeo and Maynard, 2004). However, Ti is inert to the redox change in seawater. It has a low solubility under both oxic and anoxic conditions in its dominant valance state (4+), which explains its extremely low concentration in open seawater (0.005 to 0.35 nM; Van Den Berg et al., 1994; Skrabal, 2006). Organisms have the ability to extract elements (e.g., V and P) from seawater and release them to form authigenic minerals after burial, even if the elements are present in very low concentrations (e.g., Algeo and Maynard, 2004; Yu and Wang, 2004). Unfortunately, Ti is

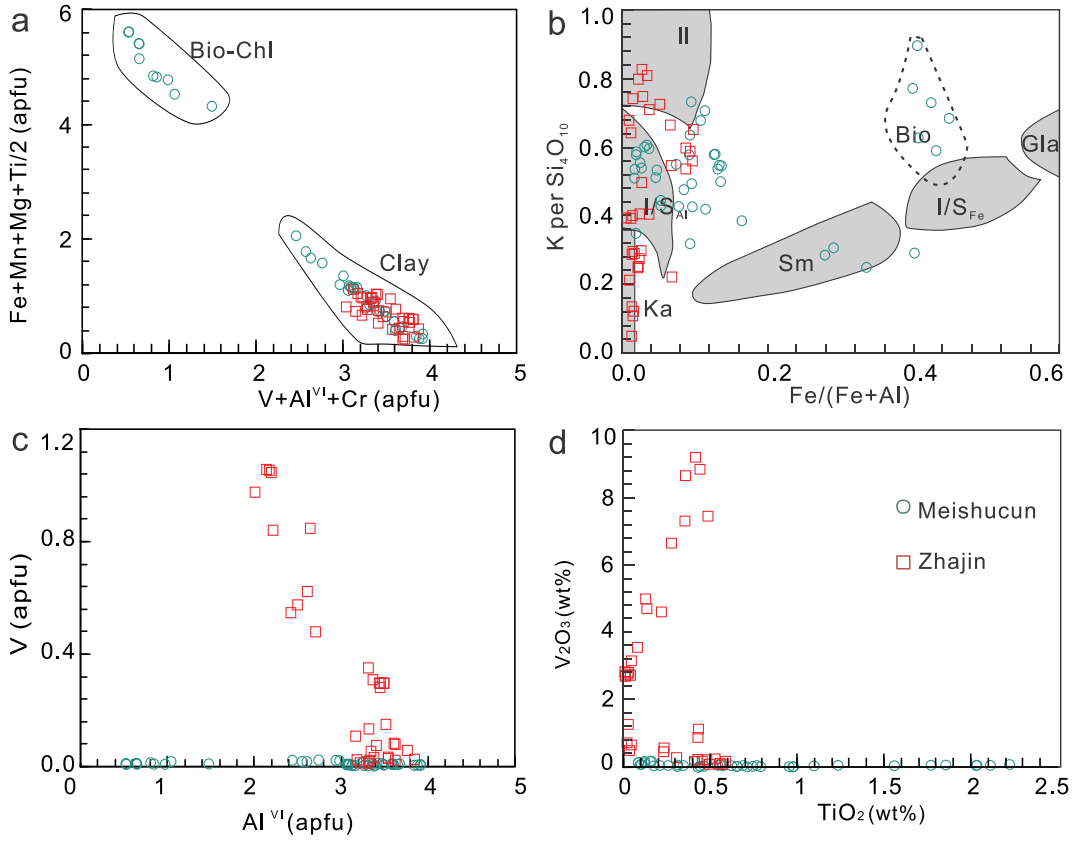

Fig. 7. Binary diagrams illustrating compositional data for the phyllosilicate minerals. In a) bio = biotite and chl = chlorite; the shaded areas in b) indicate the fields of illite (il); smectite (sm); Al-rich illite - smectite mixed layer mineral (I/S_{Al}); Fe-rich illite-smectite mixed layer mineral (I/S_{Fe}); and glauconite (Gla). apfu = atoms per formula unit.

not an essential element for life, and thus cannot be accumulated biologically as authigenic titania minerals.

Titanium-bearing minerals, such as biotite and amphibole, can be carried as detritus into oceans, and subsequently accumulate in fine-grained clastic sediments. It is possible that authigenic titania minerals form from these minerals, particularly from igneous and metamorphic biotite, which may contain several weight percents of TiO_2 (Henry and Guidott, 2002). Indeed, this would be the case for black shales of the Meishucum section, in which the only authigenic titania mineral, brookite, occurs exclusively along cleavages in relics of detrital biotite (Fig. 2c–g). Based on the association of brookite with illite or illite-smectite and biotite relicts, we propose that biotite was decomposed to form clay minerals during diagenesis, thereby releasing Ti, which was then incorporated into brookite.

7.2. The bitumen-anatase association

In contrast to the Meishucun section, relicts of biotite or other detrital Ti-bearing minerals are not observed in black shales from the Zhajin section. However, bitumen, which formed during hydrocarbon generation and solidification, is an important phase in black shales from the Zhajin section and is closely associated with anatase. Furthermore, the bitumen contains appreciable Ti (up to 1 wt%; Table 3 and Supplementary Table A1). It is thus reasonable to argue that hydrocarbon liquids released during diagenesis played a key role in transport and deposition of Ti. Fuchs et al. (2015) noted that anatase nano-crystals in the Witwatersrand Carbon Leader Reef occur within bitumen masses rather than along their borders, consistent with their precipitation from liquid hydrocarbons. By contrast, in the Zhajin section, anatase aggregates either around or inter-mingled with bitumen, arguing against dissolution and transport of Ti in a hydrocarbon liquid.

Anatase and bitumen have also been reported to occur at the oil-water interface in an oil field (Schulz et al., 2016). Oil-water interfaces are locations of very low pH (< 3–7) in the aqueous phase due to the anaerobic degradation of the oil and the resulting production of methane, carbon dioxide and acetic acid (Schulz et al., 2016). Aqueous fluids at such interfaces could be very effective in dissolving Ti-minerals in the host shales by forming stable Ti-organic complexes. Low pH and the anaerobic degradation of the oil would also promote formation and aggregation of nano-crystal titania (Chen et al., 2012; Schulz et al., 2016). However, due to the very low porosity of black shales, it is difficult to envisage a large-scale migration of oil and water and the formation of an oil-water interface in such rocks.

On the other hand, the release of diagenetic acids such as acetic or oxalic acid during the formation of hydrocarbons would decrease pore-water pH, generating a micro-environment that is favorable for the dissolution of Ti-bearing minerals (Schulz et al., 2016). The organic acids could also form chelation complexes with Ti^{4+}, which promotes migration of Ti in pore waters. In the Zhajin section, anatase occurs as sponge-like aggregates, which are likely precipitated in pore water cavities. It is thus possible that low-pH pore water with abundant organic acids released during diagenesis played a key role in dissolution and transport of Ti.

Titanium could also have been transported by and deposited from

Table 2
Major elemental compositions of clay minerals in black shales from the Meishucun and Zhajin sections, South China.

Location	Meishucun section																		
Sample no.	B9-2-1	B9-2-2	B9-2-3	B9-2-4	B9-8-1	B9-8-2	B9-8-3	B9-8-4	B9-16-1	B9-16-2	B9-2-11	B9-2-12	B9-2-13	B9-2-14	B9-6-1	B9-6-2	B9-6-3	B9-6-4	B9-6-5	B9-6-6
Description	Bi-Chl	Bi-Chl	Bi-Chl	Bi-Chl	Bi-Chl	Bi-Chl	Bi-Chl	Bi-Chl	Bi-Chl	Bi-Chl	Ill-Sm	Ill-Sm	Ill-Sm	Ill-Sm	Ill-Sm	Ill-Sm	Ill-Sm	Ill-Sm	Ill-Sm	Ill-Sm
SiO_2	35.6	36.2	35.4	32.7	35.1	33.2	34.6	33.4	31.6	30.0	47.7	49.3	45.3	48.2	47.0	47.2	53.4	52.9	53.2	56.2
TiO_2	4.24	1.23	2.02	1.55	2.02	1.84	2.10	1.76	1.09	2.21	0.56	0.62	0.65	0.57	0.26	0.21	0.16	0.41	0.12	0.09
Al_2O_3	19.0	20.2	14.4	17.8	16.8	17.2	18.1	17.4	17.6	18.5	32.5	35.0	35.0	32.2	28.5	30.5	20.6	18.9	19.8	19.1
Cr_2O_3	0.08	0.10	0.09	0.08	0.05	0.05	0.06	0.05	0.02	0.02	0.05	0.03	0.05	0.03	0.03	0.02	0.06	0.07	0.14	0.13
V_2O_3	0.12	0.06	0.06	0.05	0.05	0.07	0.06	0.06	0.04	0.08	0.07	0.05	0.02	0.05	0.05	0.05	0.19	0.18	0.14	0.14
FeO	11.0	11.0	13.6	20.4	17.4	18.4	16.9	16.8	12.5	17.7	1.30	1.00	1.00	1.2	1.6	1.4	3.8	5.3	3.0	2.9
MnO	0.07	0.05	0.09	0.01	0.21	0.15	0.21	0.22	0.13	0.28	0.01	0.01	0.03	0.00	0.01	0.00	0.01	0.02	0.00	0.00
MgO	12.2	11.8	15.0	7.3	11.5	11.6	10.3	12.6	15.7	8.50	1.40	1.00	0.70	1.3	0.9	1.2	5.5	6.8	6.3	7.2
CaO	0.29	0.39	0.18	0.29	0.30	0.27	0.34	0.21	3.38	0.86	0.23	0.09	0.27	0.26	0.28	0.61	0.24	0.24	0.44	0.34
BaO	0.03	0.02	0.02	0.11	0.17	0.05	0.16	0.07	0.00	0.14	0.26	0.30	0.29	0.28	0.12	0.14	0.00	0.02	0.00	0.00
Na_2O	0.17	0.20	0.07	0.18	0.04	0.09	0.02	0.04	0.06	0.13	0.48	0.34	0.51	0.59	0.41	0.55	0.05	0.07	0.05	0.01
K_2O	2.85	2.70	2.70	5.85	6.71	5.12	6.98	5.48	2.06	7.04	6.72	4.50	6.95	6.99	7.32	7.41	5.85	5.34	6.86	6.26
Total	85.7	84.0	83.6	86.3	90.4	87.9	89.8	88.2	84.3	85.4	91.2	92.3	90.8	91.6	86.4	89.2	89.8	90.3	90.0	92.4
Formula	O = 22																			
Si	5.54	5.71	5.76	5.47	5.54	5.36	5.48	5.36	5.15	5.11	6.47	6.48	6.20	6.52	6.76	6.59	7.38	7.34	7.37	7.53
Al^{IV}	2.46	2.29	2.24	2.53	2.46	2.64	2.52	2.64	2.85	2.89	1.53	1.52	1.80	1.48	1.24	1.41	0.62	0.66	0.63	0.47
Al^{VI}	1.04	1.48	0.52	0.97	0.65	0.64	0.84	0.65	0.53	0.80	3.67	3.92	3.84	3.65	3.60	3.61	2.74	2.44	2.61	2.55
Ti	0.50	0.15	0.25	0.20	0.24	0.22	0.25	0.21	0.13	0.28	0.06	0.06	0.07	0.06	0.03	0.02	0.02	0.04	0.01	0.01
Cr	0.01	0.01	0.01	0.01	0.01	0.01	0.01	0.01	0.00	0.00	0.01	0.00	0.01	0.00	0.00	0.00	0.01	0.01	0.02	0.01
V	0.02	0.01	0.01	0.01	0.01	0.01	0.01	0.01	0.01	0.01	0.01	0.01	0.00	0.01	0.01	0.01	0.02	0.02	0.02	0.02
Fe	1.43	1.45	1.85	2.86	2.30	2.48	2.24	2.26	1.71	2.52	0.14	0.11	0.12	0.13	0.19	0.16	0.44	0.61	0.34	0.32
Mn	0.01	0.01	0.01	0.00	0.03	0.02	0.03	0.03	0.02	0.04	0.00	0.00	0.00	0.00	0.00	0.00	0.00	0.00	0.00	0.00
Mg	2.83	2.78	3.63	1.82	2.70	2.80	2.43	3.01	3.82	2.14	0.28	0.19	0.14	0.27	0.19	0.25	1.13	1.41	1.31	1.44
Ca	0.05	0.07	0.03	0.05	0.05	0.05	0.06	0.04	0.59	0.16	0.03	0.01	0.04	0.04	0.04	0.09	0.04	0.04	0.07	0.05
Ba	0.00	0.00	0.00	0.01	0.01	0.00	0.01	0.00	0.00	0.01	0.01	0.02	0.02	0.01	0.01	0.01	0.00	0.00	0.00	0.00
Na	0.05	0.06	0.02	0.06	0.01	0.03	0.01	0.01	0.02	0.04	0.13	0.09	0.13	0.15	0.11	0.15	0.01	0.02	0.01	0.00
K	0.57	0.54	0.56	1.25	1.35	1.06	1.41	1.12	0.43	1.53	1.16	0.76	1.21	1.21	1.34	1.32	1.03	0.94	1.21	1.07

Location	Meishucun section																		
Sample no.	B9-8-11	B9-8-12	B9-8-13	B9-8-14	B9-8-15	B9-8-16	B9-8-17	B9-8-18	B9-8-19	B9-8-20	B9-8-21	B9-13-1	B9-13-2	B9-13-3	B9-16-12	B9-16-13	B9-16-14	B9-16-15	B9-16-16
Description	Ill-Sm	Ill-Sm	Ill-Sm	Ill-Sm	Ill-Sm	Ill-Sm	Ill-Sm	Ill-Sm	Ill-Sm	Ill-Sm	Ill-Sm	Ill-Sm	Ill-Sm	Ill-Sm	Ill-Sm	Ill-Sm	Ill-Sm	Ill-Sm	Ill-Sm
SiO_2	53.6	53.8	52.6	50.9	48.6	46.9	46.9	46.0	47.9	49.2	48.4	48.8	48.7	49.8	47.1	48.3	48.1	50.6	50.8
TiO_2	0.13	0.16	0.11	0.10	0.54	0.97	0.95	0.98	0.74	0.18	0.79	0.77	0.69	0.65	0.71	0.44	0.31	0.44	0.47
Al_2O_3	20.8	22.6	27.7	28.2	26.3	29.3	29.5	28.2	26.6	29.1	26.5	25.9	25.3	24.8	27.2	35.6	35.9	30.2	30.1
Cr_2O_3	0.09	0.11	0.05	0.09	0.02	0.00	0.00	0.01	0.02	0.01	0.04	0.01	0.03	0.03	0.03	0.03	0.05	0.08	0.05
V_2O_3	0.17	0.17	0.09	0.08	0.06	0.01	0.02	0.02	0.03	0.04	0.02	0.05	0.05	0.03	0.01	0.03	0.02	0.03	0.03
FeO	2.5	3.3	2.2	2.2	4.8	5.0	4.3	4.2	5.5	4.2	5.7	5.6	5.6	5.5	5.6	0.9	0.9	2.1	2.1
MnO	0.00	0.01	0.00	0.02	0.05	0.04	0.05	0.03	0.01	0.04	0.01	0.01	0.01	0.00	0.00	0.01	0.00	0.02	0.01
MgO	4.3	4.7	2.4	2.3	2.4	1.0	0.8	1.1	2.0	1.9	2.1	2.1	2.1	2.4	2.1	0.6	0.7	1.9	1.9
CaO	0.25	0.28	0.24	0.18	0.16	0.15	0.14	0.36	0.12	0.16	0.19	0.12	0.11	0.10	0.06	0.11	0.10	0.14	0.21
BaO	0.01	0.03	0.07	0.11	0.28	0.13	0.16	0.12	0.08	0.17	0.08	0.11	0.10	0.13	0.13	0.20	0.20	0.53	0.38
Na_2O	0.07	0.07	0.20	0.14	0.13	0.17	0.24	0.22	0.18	0.11	0.14	0.16	0.12	0.11	0.13	0.67	0.73	0.18	0.25
K_2O	5.99	4.49	6.12	5.72	8.98	8.31	7.79	8.80	7.26	7.44	6.79	6.99	6.95	6.51	7.12	6.77	6.41	7.07	6.80

(*continued on next page*)

Table 2 (*continued*)

Location	Meishucun section																	
Sample no.	B9-8-11	B9-8-12	B9-8-13	B9-8-14	B9-8-15	B9-8-16	B9-8-17	B9-8-18	B9-8-19	B9-8-20	B9-8-21	B9-13-1	B9-13-2	B9-13-3	B9-16-12	B9-16-13	B9-16-14	B9-16-15	B9-16-16
Description	Ill-Sm	Ill-Sm	Ill-Sm	Ill-Sm	Ill-Sm	Ill-Sm	Ill-Sm	Ill-Sm	Ill-Sm	Ill-Sm	Ill-Sm	Ill-Sm	Ill-Sm	Ill-Sm	Ill-Sm	Ill-Sm	Ill-Sm	Ill-Sm	Ill-Sm
Total	87.9	89.8	91.7	90.1	92.4	92.0	90.8	90.0	90.6	92.6	90.7	90.7	89.8	90.1	90.1	93.7	93.4	93.4	93.1
Formula	O = 22																		
Si	7.50	7.34	7.04	6.94	6.75	6.51	6.54	6.54	6.73	6.70	6.76	6.83	6.87	6.98	6.64	6.36	6.33	6.75	6.76
Al^{IV}	0.50	0.66	0.96	1.06	1.25	1.49	1.46	1.46	1.27	1.30	1.24	1.17	1.13	1.02	1.36	1.64	1.67	1.25	1.24
Al^{VI}	2.94	2.98	3.42	3.47	3.06	3.31	3.40	3.27	3.13	3.36	3.12	3.10	3.08	3.07	3.16	3.88	3.91	3.49	3.49
Ti	0.01	0.02	0.01	0.01	0.06	0.10	0.10	0.10	0.08	0.02	0.08	0.08	0.07	0.07	0.08	0.04	0.03	0.04	0.05
Cr	0.01	0.01	0.00	0.01	0.00	0.00	0.00	0.00	0.00	0.00	0.00	0.00	0.00	0.00	0.00	0.00	0.00	0.01	0.00
V	0.02	0.02	0.01	0.01	0.01	0.00	0.00	0.00	0.00	0.00	0.00	0.01	0.01	0.00	0.00	0.00	0.00	0.00	0.00
Fe	0.29	0.38	0.25	0.26	0.55	0.58	0.50	0.50	0.65	0.47	0.66	0.66	0.67	0.64	0.66	0.10	0.10	0.24	0.23
Mn	0.00	0.00	0.00	0.00	0.01	0.00	0.01	0.00	0.00	0.00	0.00	0.00	0.00	0.00	0.00	0.00	0.00	0.00	0.00
Mg	0.90	0.96	0.48	0.47	0.50	0.20	0.17	0.23	0.43	0.39	0.44	0.44	0.45	0.50	0.45	0.13	0.14	0.37	0.38
Ca	0.04	0.04	0.03	0.03	0.02	0.02	0.02	0.05	0.02	0.02	0.03	0.02	0.02	0.02	0.01	0.01	0.01	0.02	0.03
Ba	0.00	0.00	0.00	0.01	0.02	0.01	0.01	0.01	0.00	0.01	0.00	0.01	0.01	0.01	0.01	0.01	0.01	0.03	0.02
Na	0.02	0.02	0.05	0.04	0.03	0.05	0.06	0.06	0.05	0.03	0.04	0.04	0.03	0.03	0.04	0.17	0.19	0.05	0.06
K	1.07	0.78	1.05	0.99	1.59	1.47	1.39	1.60	1.30	1.29	1.21	1.25	1.25	1.16	1.28	1.14	1.08	1.20	1.15

Location	Meishucun section				Zhajin section														
Sample no.	B9-16-17	B9-16-18	B9-16-19	B9-16-20	JX37-1-1	JX37-1-2	JX37-1-3	JX37-1-4	JX37-1-5	JX37-1-6	JX37-3-1	JX37-3-2	JX37-3-3	JX37-3-4	JX37-13-1	JX37-13-2	JX37-13-3	JX37-13-7	JX37-13-8	JX37-13-9
Description	Ill-Sm	Ill-Sm	Ill-Sm	Ill-Sm	Ill-Sm	Ill-Sm	Ill-Sm	Ill-Sm	Ill-Sm	Ill-Sm	Ill-Sm	Ill-Sm	Ill-Sm	Ill-Sm	Ill-Sm	Ill-Sm	Ill-Sm	Ill-Sm	Ill-Sm	Ill-Sm
SiO_2	48.3	45.4	50.0	47.7	48.9	40.1	52.1	52.1	54.3	53.2	52.1	57.2	50.2	50.4	50.7	56.6	53.5	45.7	44.7	44.4
TiO_2	0.35	0.31	0.09	0.43	0.23	0.24	0.31	0.01	0.03	0.03	0.04	0.01	0.05	0.02	0.49	0.22	0.14	0.03	0.05	0.44
Al_2O_3	30.7	29.8	26.1	29.8	27.5	27.0	29.0	27.2	28.3	28.4	28.2	27.6	27.0	28.5	18.7	11.8	13.2	28.6	30.1	20.4
Cr_2O_3	0.02	0.02	0.02	0.02	0.22	0.18	0.39	0.27	0.30	0.27	0.25	0.38	0.28	0.24	1.09	0.67	0.65	0.27	0.15	1.37
V_2O_3	0.05	0.07	0.14	0.00	0.47	0.58	0.29	2.83	2.81	2.76	2.72	2.73	3.16	2.69	7.44	4.60	4.70	1.27	0.66	8.83
FeO	0.9	1.5	3.4	3.4	2.8	2.7	3.0	0.5	0.6	0.6	0.7	0.5	0.6	0.7	1.0	0.4	0.5	0.6	1.0	0.4
MnO	0.03	0.02	0.01	0.01	0.03	0.03	0.05	0.01	0.04	0.00	0.00	0.01	0.02	0.01	0.00	0.02	0.02	0.00	0.00	0.00
MgO	2.1	1.6	2.9	2.4	1.9	1.4	2.0	2.4	2.8	2.6	2.5	2.9	2.6	2.2	4.3	3.4	2.9	0.8	0.5	4.3
CaO	0.11	0.14	0.15	0.11	0.00	0.23	0.00	0.06	0.05	0.01	0.03	0.04	0.01	0.02	0.19	0.15	0.20	0.08	0.07	0.16
BaO	0.14	0.30	0.01	0.09	0.33	0.39	0.32	0.49	0.60	0.53	0.60	0.61	0.58	0.46	0.51	0.46	0.57	0.18	0.10	0.78
Na_2O	0.24	0.30	0.08	0.39	0.32	0.26	0.08	0.05	0.03	0.00	0.00	0.01	0.06	0.03	0.15	0.13	0.14	0.39	0.37	0.11
K_2O	7.31	7.20	6.23	6.87	6.99	6.96	3.03	3.92	1.92	1.52	1.66	0.74	3.89	3.82	5.36	3.69	3.85	8.86	9.34	4.56
Total	90.3	86.6	89.1	91.2	89.7	80.0	90.7	89.9	91.7	90.0	88.7	92.7	88.5	89.0	89.8	82.1	80.3	86.7	87.0	85.8
Formula	O = 22																			
Si	6.62	6.53	6.97	6.56	6.82	6.36	6.97	7.03	7.09	7.05	7.02	7.30	6.92	6.87	7.12	8.36	8.13	6.63	6.49	6.59
Al^{IV}	1.38	1.47	1.03	1.44	1.18	1.64	1.03	0.97	0.91	0.95	0.98	0.70	1.08	1.13	0.88	0.00	0.00	1.37	1.51	1.41
Al^{VI}	3.59	3.59	3.26	3.38	3.34	3.41	3.54	3.37	3.44	3.49	3.49	3.45	3.31	3.45	2.22	2.42	2.50	3.52	3.62	2.17
Ti	0.04	0.03	0.01	0.04	0.02	0.03	0.03	0.00	0.00	0.00	0.00	0.00	0.01	0.00	0.05	0.02	0.02	0.00	0.01	0.05
Cr	0.00	0.00	0.00	0.00	0.02	0.02	0.04	0.03	0.03	0.03	0.03	0.04	0.03	0.03	0.12	0.08	0.08	0.03	0.02	0.16
V	0.01	0.01	0.02	0.00	0.05	0.07	0.03	0.31	0.29	0.29	0.29	0.28	0.35	0.29	0.84	0.55	0.57	0.15	0.08	1.05
Fe	0.10	0.18	0.40	0.39	0.33	0.36	0.34	0.06	0.06	0.07	0.07	0.06	0.07	0.08	0.12	0.05	0.06	0.07	0.12	0.05
Mn	0.00	0.00	0.00	0.00	0.00	0.00	0.01	0.00	0.00	0.00	0.00	0.00	0.00	0.00	0.00	0.00	0.00	0.00	0.00	0.00
Mg	0.43	0.35	0.59	0.49	0.40	0.34	0.41	0.49	0.54	0.52	0.50	0.55	0.54	0.45	0.89	0.74	0.66	0.16	0.12	0.96
Ca	0.02	0.02	0.02	0.02	0.00	0.04	0.00	0.01	0.01	0.00	0.00	0.01	0.00	0.00	0.03	0.02	0.03	0.01	0.01	0.02
Ba	0.01	0.02	0.00	0.00	0.02	0.02	0.02	0.03	0.03	0.03	0.03	0.03	0.03	0.02	0.03	0.03	0.03	0.01	0.01	0.05
Na	0.06	0.08	0.02	0.10	0.09	0.08	0.02	0.01	0.01	0.00	0.00	0.00	0.02	0.01	0.04	0.04	0.04	0.11	0.10	0.03

Table 2 (*continued*)

Location	Meishucun section				Zhajin section													
Sample no.	B9-16-17	B9-16-18	B9-16-19	B9-16-20	JX37-1-1	JX37-1-2	JX37-1-3	JX37-1-4	JX37-1-5	JX37-1-6	JX37-3-1	JX37-3-2	JX37-3-3	JX37-3-4	JX37-13-1	JX37-13-2	JX37-13-3	JX37-13-7	JX37-13-8	JX37-13-9
Description	Ill-Sm	Ill-Sm	Ill-Sm	Ill-Sm	Ill-Sm	Ill-Sm	Ill-Sm	Ill-Sm	Ill-Sm	Ill-Sm	Ill-Sm	Ill-Sm	Ill-Sm	Ill-Sm	Ill-Sm	Ill-Sm	Ill-Sm	Ill-Sm	Ill-Sm	Ill-Sm
K	1.28	1.32	1.11	1.20	1.24	1.41	0.52	0.68	0.32	0.26	0.29	0.12	0.68	0.67	0.96	0.69	0.75	1.64	1.73	0.86

an acidic, low-temperature hydrothermal fluid that interacted with the shales after diagenesis (Parnell, 2004). Because Nd isotopes do not fractionate, even at low temperatures (Ling et al., 1997), and the oceanic residence time of Nd (300–1000 year) is less than the oceanic mixing time (1500–2000 years) (Tachikawa et al., 2003), Nd isotopes can be used to determine whether rocks have undergone modification by post-diagenetic hydrothermal fluids. Black shales in the Meishucun and Zhajin sections have relatively constant εNd(t) values (mostly between −6.91 and −5.74), which are indicative of stable continental inputs with no involvement of hydrothermal fluids (Table 5). An exception is that a sample collected from the top of the Zhajin section that has a relatively high εNd(t) value of 0.49, which may reflect prolonged interaction with meteoric waters. We therefore conclude that anatase in the Zhajin section formed as a result of dissolution and transportation by hydrocarbon during late-diagenesis.

7.3. Growth of titania minerals

7.3.1. Precipitation of brookite and anatase

Brookite in black shales from the Meishucun section occurs along cleavages of partially decomposed detrital biotite crystals (Fig. 2). Given the very low solubility of Ti in aqueous fluids and the preferential adsorption of metal oxides (Cornu et al., 1999), Ti was predictably immobile and crystalized in situ in black shales from the Meishucun section. In contrast, Ti in the black shales from the Zhajin section was likely mobilized by the formation of stable organic complexes. Precipitation of anatase nano-crystals is inferred to have resulted from a subsequent increase in pH, which destabilized the organic Ti complexes; a temperature increase may also have been a contributing factor by destroying essential organic ligands (Schulz et al., 2016). Increasing pH was also likely responsible for the observed aggregation of the nano-crystals on the basis of the experimental results showing that adsorption of humic acids by nano-crystals of TiO_2 strongly decreases above pH values of 5 to 6, and that this decrease promotes anatase aggregation (Yang et al., 2009).

As discussed above, titania mineralization in the Zhajin section involved a role for liquid hydrocarbons, the generation of which depended on the thermal maturity and TOC content of the black shales. The assessment of thermal maturity in pre-Devonian shales is challenging due to the absence of vitrinite macerals that precludes the application of vitrinite reflectance petrography, the most-widely used assessment technique (c.f. Cheshire et al., 2017). We therefore compared the thermal maturities of black shales from the Meishucun and Zhajin sections using Rock-Eval pyrolysis data. As is the case with most Cambrian shales, black shales from the Zhajin section have very low residual petroleum potential (S_2 = 0.01–0.29 mg HC/g rock) but a very high TOC content (7 to 15 wt%). The extremely low HI values (0.1–2.0 mg HC/g TOC) for this section indicate that the black shales have a very high thermal maturity and released abundant hydrocarbons during burial and late-diagenesis. In contract, black shales from the Meishucun section have a little higher S_2 value (0.1–0.43 mg HC/g rock) and much lower TOC (1 to 4 wt%) than the black shales of the Zhajin section. The high HI values (3.8–20 mg HC/g TOC) indicate that the black shales from the Zhajin section have lower thermal maturity and still retain the potential for hydrocarbon generation. Also, the higher TOC content led to the formation relatively large pores and higher overall porosity during cracking, which accelerated the migration of Ti. Clay minerals in the black shales from the Zhajin section have much lower Fe/Al ratio and are much closer in composition to illite than clay minerals in black shales from the Meishucun section (Fig. 7b). In addition, V and Al^{VI}, are negatively correlated (Fig. 7c; Table 2), indicating the substitution of V for Al during the smectite-illite transition. This is consistent with a higher degree of hydrocarbon maturation of black shales from the Zhajin section relative to those from the Meishucun section.

Thus, we propose that, in both sections, detrital biotite was the main

Table 3
Major elemental compositions of bitumen in black shales from the Zhajin sections, South China.

Sample no.	JX37-3-21	JX37-3-22	JX37-3-23	JX37-3-24	JX37-13-25	JX37-13-26	JX37-13-27	JX37-13-28	JX37-13-29	JX37-23-21	JX37-23-22	JX37-24-23	JX37-24-24	JX37-24-25
SiO_2	15.08	2.01	11.92	50.72	2.72	0.19	0.08	1.02	10.12	8.96	14.96	0.85	0.36	7.46
TiO_2	0	0.14	0.63	0.47	0.09	0	0.01	0	0	0.83	6.45	4.33	0.55	0.82
Al_2O_3	4.48	0.21	0.11	0.26	0.14	0.02	0.02	0.14	1.38	1.91	1.46	0.23	0.22	1.58
Cr_2O_3	0.08	0.01	0	0	0	0.03	0	0.01	0.06	0.07	0.04	0.02	0	0.04
V_2O_3	0.75	0.02	0.05	0.03	0.03	0.04	0.02	0.03	0.29	0.33	0.5	0.24	0.05	0.25
FeO	0.15	0.1	0.05	0.05	0.13	0.06	0.04	0.03	0.08	0.17	0.22	0.13	0.12	0.18
MnO	0.02	0	0.01	0	0.01	0	0	0.01	0.01	0.01	0	0	0.01	0
MgO	4.27	0.02	0.01	0.01	0.03	0	0	0.02	0.24	0.23	0.18	0.06	0	0.23
CaO	0.06	0.03	0.01	0.04	0.05	0.02	0.02	0.02	0.04	0.05	0.08	0.03	0.02	0.14
Na_2O	0	0.02	0	0.01	0.03	0.01	0.03	0.04	0.08	0.11	0.08	0.03	0.04	0.1
K_2O	0.35	0.03	0	0.02	0.02	0.01	0.01	0.03	0.4	0.54	0.34	0.04	0.02	0.41
Total	25.29	2.61	12.8	51.61	3.28	0.37	0.22	1.36	12.7	13.21	24.3	5.96	1.38	11.21

source of Ti and partially decomposed during early diagenesis, forming tabular authigenic brookite crystals within the relict grains. In black shales from the Zhajin section, however, the greater maturity of the organic matter and high TOC content led to the generation of abundant liquid hydrocarbons, which interacted locally with pore waters reducing their pH, thereby destroying the relict biotite grains and enabling mobilization of the authigenic brookite (and Ti in biotite) as aqueous organic Ti complexes. These complexes, as discussed above, were subsequently destabilized to form anatase nano-crystals and, in turn, sponge-like aggregates of anatase nano-crystals.

7.3.2. Controls on crystallization of brookite and anatase

According to Schulz et al. (2016), anatase is the first titania phase to crystallize from aqueous solutions (as nano-crystals) as its surface energy is lower than that of brookite. However, it can be readily converted to brookite during growth. One of the mechanisms is the nucleation of brookite from the twin planes of anatase which has a similar structure to that of brookite (Zhang and Banfield, 2014). In sol-gel experiments designed to synthesize nano-crystalline TiO_2, anatase is the dominant phase if the crystals are < 11 nm in diameter, whereas brookite dominates when the crystals are between 11 and 35 nm in diameter and rutile forms when the crystal size is > 35 nm (Zhang and Banfield, 2014). However, micron-size crystals of both anatase and brookite are observed in black shales (Cabral et al., 2012; Parnell, 2004; Schulz et al., 2016). It has therefore been suggested that, in natural environments, the stability and growth of titania are mainly controlled by pH, with brookite formation favored at moderately acidic pH (3–6) and anatase at high pH (> 5) (Zhang and Banfield, 2014). These findings are consistent with the observation that brookite in the Meishucun section crystallized in a micro-environment with abundant HS^- (acidic), and anatase precipitated rapidly in black shales of the Zhajin section after destabilization of organo-Ti complexes as pH increased to near neutral values.

Dopants in the titania change its lattice and thus can lead to the formation of different phases. For example, in sol-gel syntheses of titania, it has been observed that elevated concentrations of Mo^{6+} lead to the transformation of brookite to anatase, whereas high concentrations of Fe^{3+} and V^{5+} favor the formation of brookite (Khan and Berk, 2014). In contrast, it has been shown that incorporation of V^{4+} leads to the preferential formation of anatase (Li et al., 2010). Although these two studies were undertaken at different temperatures (300 °C/500°Cand 50 °C, respectively) using different inorganic Ti precursors (Ti oxysulfate vs. tetrabutyl titanate), the results suggest that the incorporation of V with lower valance in the second study may be the reason for the formation of anatase rather than brookite (Li et al., 2010). In our study, both brookite in black shales from the Meishucun section and anatase in black shales from the Zhajin section contain abundant V (> 1 wt% V_2O_3). As discussed above, brookite in the Meishucun section precipitated within pore water, whereas the formation of anatase in black shales from the Zhajin section was closely linked to the generation of organic-rich liquids after burial. Significantly, V in crude oils occurs mainly as V^{4+} (Baranova and Fortunatov, 2012; Mandal et al., 2014), which may be a reason why anatase was favored over brookite in black shales from Zhajin. By analogy, it is therefore possible that V in black shales from Meishucun was mostly present as V^{5+}, thereby favoring the precipitation of brookite. Thus, different pH and/or valance state of V may be the reason that authigenic titania occurs as brookite in the Meishucun black shales and as anatase in the Zhajin black shales.

7.4. Implications for the reliability of redox proxies

The geochemistry of marine black shales, including the concentration of redox sensitive elements (RSEs; e.g., Mo, U and V), the ratios of V/V + Ni and the Fe speciation, have long been taken as important proxies for paleo-environmental conditions (e.g., Algeo and Maynard, 2004; Anderson and Raiswell, 2004; Tribovillard et al., 2006). Recent studies, however, have demonstrated that multiple geochemical proxies may yield conflicting redox interpretations. For example, early Ediacaran black shales from the Yanjia section, South China, have highly variable Fe speciation and enrichment of RSEs, suggesting that redox conditions varied from oxic to euxinic, whereas their persistently high TOC/P ratios argue for an anoxic dominated depositional environment (Jin et al., 2018). Similarly, early Cambrian black shales from the Hetang Formation have high but variable RSEs/TOC ratios, which are indictive of a euxinic depositional environment but conflict with the presence of oxygen-dependent sponge species in the shales (Cheng et al., 2017). Although the high variability in the values of geochemical redox proxies has been attributed to transient redox changes (Cheng et al., 2017), or different sensitivities of the elements to high-frequency redox fluctuations (Jin et al., 2018), the driving forces for the transient or high-frequency redox changes are unclear.

Mobilization of the normally inert element, Ti, in black shales from the Zhajin section provides evidence for the re-distribution of trace

Table 4
Total organic carbon (TOC), rock-eval pyrolysis and trace elemental compositions of black shales from the Meishucun and Zhajin sections, South China.

Location	Meishucun section														
Sample	B9-1	B9-2	B9-5	B9-6	B9-8	B9-10	B9-13	B9-15	B9-16	B9-20	B9-25	B9-30	B9-35	B9-36	B9-39
TOC	3.9	2.0	3.2	2.9	2.7	2.6	2.6	3.1	2.0	3.7	3.4	2.3	3.1	2.2	3.0
S1	0.04	0.12	0.12	0.15	0.05			0.16		0.06	0.24	0.09	0.12		0.09
S2	0.15	0.4	0.26	0.43	0.13			0.29		0.21	0.37	0.16	0.23		0.17
HI	3.8	20.0	8.1	14.8	5.0			9.4		5.7	10.9	7.0	7.4		5.7
Ti	4790	5647	5569	5366	5443	5234	5437	3345	5683	5132	5168	5623	5294	5401	5234
Sc	16.4	17.5	16.2	15.7	16.3	15.1	15.6	14.9	15.3	13.9	14.4	15.3	15.2	15.0	15.1
V	312	178	458	528	437	555	300	98.0	305	277	273	124	127	119	154
Cr	232	150	262	255	226	186	174	60.0	139	107	100	92.0	94.0	92.0	101
Co	9.88	14.3	15.4	15.8	14.5	15.2	13.9	10.9	16.1	13.2	14.4	16.7	17.5	17	16
Ni	59.1	66.3	84.9	85.6	64.2	68.0	74.1	39.2	71.9	70.2	68.3	61.1	56.0	53.5	66.1
Cu	41.4	27.8	42.8	42.4	53.2	36.8	34.8	19.7	32.00	28.2	35.00	32.7	40.4	34.3	45.3
Zn	92.7	65.7	78.7	88.4	88.8	97.9	88.1	54.8	83.9	75.7	82.9	78.3	96.0	82.9	93.3
Ga	15.8	16.5	19.3	18.9	19.4	18.8	18.5	12.6	18.4	17.7	17.2	17.8	18.8	17.6	19.7
Rb	120	120	126	125	128	123	123	80.0	125	119	113	115	125	116	127
Sr	58.6	55.9	64.8	64.4	73.0	64.3	70.4	80.2	62.2	95	73.4	65.4	77	65.1	78.5
Y	32.0	25.7	32.2	32.2	36.8	30.6	32.1	45.5	26.4	38.1	35.7	29.5	32.6	27.7	34.4
Zr	161	177	190	172	186	169	184	99.3	197	192	184	227	214	216	203
Nb	11.7	11.8	12.7	12.1	13.4	12.4	12.8	8.36	12.7	12.4	12.1	13.5	13.5	12.9	13.4
Cs	9.26	8.01	8.08	7.98	7.91	7.32	7.12	4.88	6.73	6.88	6.36	5.88	6.78	5.85	6.92
Ba	563	556	517	535	489	485	480	316	584	521	584	601	562	595	538
La	37.5	35.0	32.2	28.4	37.1	29.5	32.9	25.3	31.0	32.6	29.7	31.6	45.1	32.3	41.5
Ce	60.5	63.8	58.00	50.3	65.00	51.8	56.9	46.3	54.3	58.0	53.6	59.7	83.2	59.4	79.6
Pr	6.72	6.66	7.06	6.34	7.77	6.2	6.86	6.12	6.34	7.17	6.68	6.81	10.2	6.71	9.49
Nd	23.6	23	25.9	24.1	30.9	23.8	25.8	26.7	23.0	28.7	25.7	26.0	37.1	24.9	35.8
Sm	4.26	3.96	4.61	5.06	5.66	4.5	4.56	6.03	3.78	5.85	5.43	4.45	5.86	4.12	5.95
Eu	0.73	0.69	0.91	1.08	1.11	0.94	0.93	1.37	0.79	1.32	1.17	0.88	1.09	0.86	1.24
Gd	4.09	3.8	4.42	4.81	5.50	4.44	4.56	6.04	3.75	6.16	5.62	4.2	5.35	3.89	5.76
Tb	0.62	0.57	0.65	0.70	0.79	0.63	0.65	0.94	0.53	0.88	0.81	0.6	0.73	0.57	0.80
Dy	3.71	3.4	4.13	4.16	4.70	3.95	4.04	5.88	3.33	5.11	4.83	3.84	4.45	3.59	4.79
Ho	0.82	0.72	0.8	0.84	0.92	0.78	0.80	1.16	0.69	0.99	0.93	0.79	0.89	0.76	0.95
Er	2.50	2.23	2.51	2.46	2.69	2.31	2.40	3.34	2.13	2.96	2.68	2.39	2.63	2.35	2.92
Tm	0.37	0.35	0.35	0.34	0.40	0.33	0.34	0.47	0.32	0.41	0.37	0.34	0.37	0.33	0.39
Yb	2.21	2.14	2.37	2.26	2.53	2.16	2.25	2.98	2.12	2.63	2.42	2.29	2.46	2.30	2.70
Lu	0.35	0.34	0.34	0.33	0.37	0.32	0.33	0.43	0.31	0.40	0.35	0.34	0.37	0.33	0.38
Hf	3.77	4.07	4.38	3.83	4.40	4.00	4.12	2.31	4.67	4.43	4.29	5.36	5.09	5.15	4.95
Ta	0.72	0.70	1.00	0.94	1.03	1.00	1.03	0.72	0.92	0.94	0.92	1.05	1.05	1.03	1.02
Pb	19.7	19.4	13.5	15.6	11.5	10.7	9.80	6.80	11.3	11.2	10.1	11.5	18.3	15.1	12.2
Th	10.1	10.1	9.88	8.78	10.2	8.85	9.44	5.94	9.45	9.65	9.32	10.5	11.00	10.6	10.8
U	12.5	7.30	9.20	12.1	9.70	9.80	10.1	7.70	10.2	13.3	10.7	9.6	15.8	11.0	12.4
Ge	1.07	1.11	1.39	1.33	1.54	1.47	1.68	0.84	1.34	1.27	1.33	1.37	1.38	1.25	1.45
Ni/Co	6.0	4.6	5.5	5.4	4.4	4.5	5.3	3.6	4.5	5.3	4.7	3.7	3.2	3.1	4.1
U/Th	1.2	0.7	0.9	1.4	0.9	1.1	1.1	1.3	1.1	1.4	1.1	0.9	1.4	1.0	1.1
V/TOC	81	88	144	180	164	212	118	32	154	75	81	55	40	55	52
V/Cr	1.3	1.2	1.7	2.1	1.9	3.0	1.7	1.6	2.2	2.6	2.7	1.4	1.4	1.3	1.5
V/V + Ni	0.8	0.7	0.8	0.9	0.9	0.9	0.8	0.7	0.8	0.8	0.8	0.7	0.7	0.7	0.7

Location	Meishucun section	Zhajin section													
Sample	B9-40	JX-37-1	JX-37-3	JX-37-9	JX-37-13	JX-37-14	JX-37-17	JX-37-19	JX-37-21	JX-37-23	JX-37-24	JX-37-38	JX-37-40	JX-37-42	JX-37-45
TOC	1.6	14.8	11.6	7.1	11.3	12.7	13.5	15.1	15.5	13.1	14.2	13	11.9	15.6	13.7
S1	0.05	0.06	0.05	0.14	0.1	0.05	0.01	0.11	0.11	0.04	0.12	0.01	0.1	0.01	0.04

(*continued on next page*)

Table 4 (*continued*)

Location	Meishucun section	Zhajin section													
Sample	B9-40	JX-37-1	JX-37-3	JX-37-9	JX-37-13	JX-37-14	JX-37-17	JX-37-19	JX-37-21	JX-37-23	JX-37-24	JX-37-38	JX-37-40	JX-37-42	JX-37-45
S2	0.1	0.08	0.06	0.03	0.23	0.09	0.01	0.2	0.29	0.07	0.24	0.02	0.18	0.02	0.07
HI	6.3	0.5	0.5	0.4	2.0	0.7	0.1	1.3	1.9	0.5	1.7	0.2	1.5	0.1	0.5
Ti	4916	2047	2434	1737	2313	1879	1130	1831	1278	988	1212	3293	1767	1939	1779
Sc	13.8	10.0	12.6	8.99	9.68	7.21	5.76	9.44	6.03	4.51	5.21	16.16	8.73	14.56	9.55
V	136	7740	7390	7699	5676	3085	6925	5920	2950	6002	6336	4690	6110	4890	10,382
Cr	90.0	781	1221	595	211	148	973	502	244	355	126	264	644	250	944
Co	17.1	9.78	10.3	8.24	10.8	15.4	7.39	9.62	12.3	2.20	4.87	14.8	15.0	1.56	0.47
Ni	55.5	272	294	225	218	178	220	205	153	81.7	162	276	288	78.1	41.6
Cu	28.8	461	280	368	75.8	51.1	644	181	182	80.0	101	98.6	414	54.5	266.9
Zn	80.7	6560	6940	6544	832	107	4025	4980	280	22.6	25.9	893	3650	19.3	22.2
Ga	17.8	9.54	11.8	13.3	11.4	8.29	9.56	9.96	7.55	8.17	8.78	11.4	9.81	9.18	14.03
Rb	113	60.0	67.0	82.0	82.0	73.0	62.0	60.0	59.0	51.0	59.0	82.0	65.0	45.0	81.0
Sr	59.7	19.00	24.8	26.8	40.9	31.7	24.5	24.6	53.8	25.4	27.3	39.9	28.5	22.1	11.4
Y	23.6	31.5	41.4	38.3	46.1	25.7	61.6	35.5	33.5	17.8	27.7	39.5	33.0	31.1	35.7
Zr	174	43.2	49.5	50.4	60.8	52.0	41.7	37.3	40.4	37.6	37.7	57.4	42.8	42.1	58.2
Nb	11.9	4.47	5.36	5.96	7.56	7.00	4.31	4.13	5.17	3.81	4.29	8.19	4.73	4.58	6.09
Cs	4.88	15.7	18.8	15.3	20.6	14.7	18.1	11.9	14.5	10.6	13.9	18.9	16.9	4.94	10.2
Ba	553	1120	1350	2771	7841	10,394	1469	1700	5204	1260	1480	6550	1270	1510	2437
La	23.7	11.4	28.1	12.7	31.2	8.17	11.2	16.3	16.0	11.1	17.0	29.6	12.3	18.2	14.8
Ce	43.9	10.6	25.3	13.4	34.9	9.90	11.7	16.5	15.9	10.0	16.5	32.6	12.9	16.7	16.8
Pr	5.15	1.93	4.82	3.02	6.53	2.21	2.97	3.26	3.78	2.13	3.84	5.51	2.53	3.02	3.56
Nd	19.3	8.50	20.1	13.7	25.4	16.1	15.0	14.7	16.4	8.90	16.8	21.9	11.4	14.5	14.4
Sm	3.68	1.94	3.68	3.28	4.94	2.50	4.03	3.09	3.33	1.92	3.83	3.84	2.56	2.5	3.17
Eu	0.77	0.47	0.76	0.66	0.85	0.34	1.01	0.68	0.64	0.40	0.78	0.74	0.55	0.51	0.63
Gd	3.37	2.48	4.23	3.77	5.30	2.76	5.30	3.62	3.72	1.99	4.07	4.16	3.09	2.73	3.30
Tb	0.52	0.40	0.64	0.64	0.78	0.46	0.90	0.56	0.59	0.32	0.62	0.62	0.50	0.44	0.61
Dy	3.17	3.10	4.26	4.43	5.10	3.14	6.27	4.07	3.91	2.18	3.87	4.28	3.51	2.98	4.33
Ho	0.64	0.79	1.07	1.12	1.22	0.76	1.65	0.99	0.95	0.54	0.89	1.02	0.87	0.75	1.08
Er	1.96	2.28	3.20	3.45	3.56	2.29	5.01	2.82	2.76	1.69	2.50	3.10	2.55	2.25	3.37
Tm	0.28	0.38	0.49	0.52	0.52	0.34	0.71	0.44	0.41	0.26	0.36	0.46	0.43	0.34	0.52
Yb	1.99	2.28	3.01	3.30	3.24	2.17	4.24	2.74	2.58	1.71	2.24	2.92	2.61	2.11	3.47
Lu	0.29	0.36	0.45	0.54	0.51	0.33	0.66	0.40	0.40	0.27	0.35	0.44	0.39	0.31	0.55
Hf	4.12	0.89	1.10	1.53	1.66	1.44	1.10	0.85	1.15	1.02	1.04	1.24	1.04	0.93	1.49
Ta	0.83	0.23	0.29	0.43	0.49	0.44	0.28	0.20	0.33	0.26	0.31	0.39	0.23	0.23	0.4
Pb	8.2	43.3	41.1	41.7	26.8	29.4	28.5	38.8	32.0	24.3	18.2	45.4	46.3	29.8	58.1
Th	8.86	3.19	3.78	5.76	6.47	6.16	3.79	3.38	4.22	3.52	4.04	6.09	3.54	3.47	5.21
U	4.4	38.4	47	65.5	53.2	36.9	53.7	31.4	54.1	34.4	53.2	38.7	40.3	28.7	88.5
Ge	1.37	2.06	2.81	1.92	2.18	1.77	1.98	1.71	1.90	1.52	1.54	1.59	2.20	1.66	2.50
Ni/Co	3.2	27.8	28.5	27.3	20.2	11.5	29.7	21.3	12.4	37.1	33.3	18.6	19.2	50.1	88.9
U/Th	0.5	12.1	12.4	11.4	8.2	6.0	14.2	9.3	12.8	9.8	13.2	6.4	11.4	8.3	17.0
V/TOC	84	523	635	1092	505	243	515	393	190	460	448	360	514	313	758
V/Cr	1.5	9.9	6.1	12.9	26.8	20.8	7.1	11.8	12.1	16.9	50.5	17.8	9.5	19.6	11.0
V/V + Ni	0.7	1.0	1.0	1.0	1.0	0.9	1.0	1.0	1.0	1.0	1.0	0.9	1.0	1.0	1.0

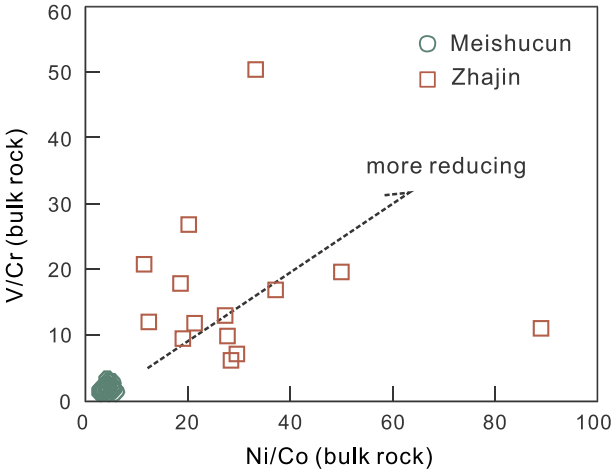

Fig. 8. Bulk rock Ni/Co vs. V/Cr plot showing the depositional redox states of black shales from the Meishucun and Zhajin sections.

are likely to record relatively reliable redox information. For example, black shales in the Zhajin section exhibit a large variation of V/Cr and Ni/Co ratios which are likely attributed to redox variation during deposition or late-diagenetic migration (Fig. 8). But our overarching conclusion for these black shales can be easily reached by their average compositions, i.e., these black shales were deposited in a more reducing environment than those from the Meishucun section (Fig. 8; Hatch and Leventhal, 1992; Jones and Manning, 1994). In conclusion, the study does not deny the applications of these proxies on high thermal maturity black shales, but transient or high-frequency changes in RSEs and Fe species should cause special attention.

8. Conclusions

Detrital biotite was the major source of Ti for the authigenic titania in early Cambrian black shales, South China. During early diagenesis, Ti in black shales was immobile and precipitated in situ as brookite. However, the generation of hydrocarbon liquids can lead to complete destruction of the Ti-bearing minerals and the mobilization of Ti due to the formation of organic-Ti complexes. These liquids precipitated nano-

Table 5
Nd isotopic compositions of black shales from the Meinshucun and Zhajin sections, South China.

Sample	Age (Ma)	Sm [ppm]	Nd [ppm]	147Sm/144Nd	143Nd/144Nd	(1σ)	(143Nd/144Nd)I	εNd(t)
Meishucun section								
B9-1	525	4.26	23.6	0.113962	0.51205	4.49E−06	0.511658	−5.93
B9-5	525	4.61	25.9	0.112373	0.512054	4.62E−06	0.511668	−5.74
B9-10	525	4.5	23.8	0.11937	0.512052	4.22E−06	0.511641	−6.25
B9-20	525	5.85	28.7	0.128687	0.512066	3.26E−06	0.511623	−6.60
B9-30	525	4.45	26	0.108056	0.512015	2.50E−06	0.511643	−6.21
B9-40	525	3.68	19.3	0.120379	0.512039	3.74E−06	0.511625	−6.57
Zhajin section								
JX-37-14	525	2.50	16.1	0.098256	0.51196	7.52E−06	0.511622	−6.63
JX-37-17	525	4.03	15.0	0.170043	0.512244	5.05E−06	0.511659	−5.91
JX-37-24	525	3.83	16.8	0.143796	0.512158	5.95E−06	0.511663	−5.82
JX-37-42	525	2.50	14.5	0.109132	0.511983	6.70E−06	0.511608	−6.91
JX-37-45	525	3.17	14.4	0.13936	0.512466	5.94E−06	0.511987	0.49

elements in carbonaceous rocks during late-diagenesis. Indeed, some redox sensitive or environmentally toxic elements, including V, Ni, Fe, Cr, Zn, Mo and Hg, have been shown to be re-distribute as a result of their concentration in the organic fraction at conditions of high thermal maturity (de Souza et al., 2006; Fein and Williams-Jones, 1997). For example, bitumen in black shales from the La Luna Formation, Maracaibo Basin has V concentrations as high as 1730 ppm and higher V/V + Ni ratios relative to the host rocks (Lo Monaco et al., 2002). Similarly, Fe concentrations in crude oils and their condensates from South African Basins can be as high as 7300 ppm (Akinlua et al., 2015). The affinity of organic phases for these metals indicates that, as is the case for Ti, they are readily mobilized when hydrocarbon-rich liquids are generated in the sediments.

Owing to the extremely low permeability of black shales, liquid hydrocarbon migration is spatially limited (Gao et al., 2018). Thus, although sedimentary sequences likely exhibit increased variability in the contents of RSEs after they have interacted with hydrocarbon-rich liquids, this increase may be relatively small. A more significant effect of the interaction of these sequences with hydrocarbon liquids is the release of highly reactive Fe into the liquids through the dissolution of detritus, e.g., biotite (Fig. 2c and e), which could change the bulk-rock Fe speciation.

Nonetheless, because hydrocarbon liquids cannot migrate far in shales due to the low-porosity of the latter, the average contents of trace elements of these rocks, if established with high-resolution sampling, crystalline anatase and eventually nanocrystalline anatase aggregates in response to increasing pH. Because of the high solubility of V in liquid hydrocarbons, this also led to the incorporation of V^{4+} in the anatase structure. Our study illustrates the role that liquid hydrocarbons play in the mobilization of Ti in black shales. Finally, the study emphasizes the need to consider the possibility that many elements used as redox proxies may be re-distributed in organic-rich shales during late-diagenesis, which could potentially render them unreliable.

Acknowledgements

This research was supported financially by grants from the National Natural Science Foundation of China (41772087 and 41572170), the Research Council of Hong Kong (17306814), and the “CAS Hundred Talents” Project to J.F. Gao. We thank Dr. Wen Zhao for his assistance in the field, Prof. Liang Qi for the trace element analysis and Dr. Xingchao Jiang for the Rock-Eval pyrolysis experiment. We appreciate the constructive comments from the journal editor (Prof. Karen Johannesson) and three reviewers (Dr. Junpeng Zhang, Dr. Arkadiusz Derkowski and an anonymous reviewer) that helped improve the paper.

Appendix A. Supplementary data

Supplementary data to this article can be found online at https://doi.org/10.1016/j.chemgeo.2018.12.022.

References

Akinlua, A., Sigedle, A., Buthelezi, T., Fadipe, O.A., 2015. Trace element geochemistry of crude oils and condensates from South African Basins. Mar. Pet. Geol. 59, 286–293.

Algeo, T.J., Maynard, J.B., 2004. Trace-element behavior and redox facies in core shales of Upper Pennsylvanian Kansas-type cyclothems. Chem. Geol. 206 (3–4), 289–318.

Anderson, T.F., Raiswell, R., 2004. Sources and mechanisms for the enrichment of highly reactive iron in euxinic Black Sea sediments. Am. J. Sci. 304 (3), 203–233.

Baioumy, H.M., 2014. Ti-bearing minerals in sedimentary kaolin deposits of Egypt. Appl. Clay Sci. 101, 345–353.

Bao, S., Zhang, Y., Hang, J., Yang, X., Hu, Y., 2012. Determination of vanadium valency in roasted stone coal by separate dissolve-potentiometric titration method. In: MRS Proceedings. Cambridge Univ Press (pp. imrc2011-1380-s21-full013).

Baranova, V.N., Fortunatov, A.V., 2012. Vanadium: chemical properties, uses and environmental effects. In: Chemical Engineering Methods and Technology. Nova Science Pub Inc.

Byrne, C., Fagan, R., Hinder, S., McCormack, D.E., Pillai, S.C., 2016. New approach of modifying the anatase to rutile transition temperature in TiO2 photocatalysts. RSC Adv. 6 (97), 95232–95238.

Cabral, A.R., Reith, F., Lehmann, B., Brugger, J., Meinhold, G., Tupinamba, M., Kwitko-Ribeiro, R., 2012. Anatase nanoparticles on supergene platinum-palladium aggregates from Brazil: titanium mobility in natural waters. Chem. Geol. 334, 182–188.

Chen, G.X., Liu, X.Y., Su, C.M., 2012. Distinct effects of humic acid on transport and retention of TiO_2 rutile nanoparticles in saturated sand columns. Environ. Sci. Technol. 46 (13), 7142–7150.

Cheng, M., Li, C., Zhou, L., Feng, L.J., Algeo, T.J., Zhang, F.F., Romaniello, S., Jin, C.S., Ling, H.F., Jiang, S.Y., 2017. Transient deep-water oxygenation in the early Cambrian Nanhua Basin, South China. Geochim. Cosmochim. Acta 210, 42–58.

Cheshire, S., Craddock, P.R., Xu, G.P., Sauerer, B., Pomerantz, A.E., McCormick, D., Abdallah, W., 2017. Assessing thermal maturity beyond the reaches of vitrinite reflectance and Rock-Eval pyrolysis: a case study from the Silurian Qusaiba formation. Int. J. Coal Geol. 180, 29–45.

Cornu, S., Lucas, Y., Lebon, E., Ambrosi, J.P., Luizao, F., Rouiller, J., Bonnay, M., Neal, C., 1999. Evidence of titanium mobility in soil profiles, Manaus, central Amazonia. Geoderma 91 (3–4), 281–295.

Emerson, S.R., Huested, S.S., 1991. Ocean anoxia and the concentrations of molybdenum and vanadium in Seawater. Mar. Chem. 34 (3–4), 177–196.

Fein, J.B., Williams-Jones, A., 1997. The role of mercury-organic interactions in the hydrothermal transport of mercury. Econ. Geol. 92 (1), 20–28.

Frank, O., Zukalova, M., Laskova, B., Kurti, J., Koltai, J., Kavan, L., 2012. Raman spectra of titanium dioxide (anatase, rutile) with identified oxygen isotopes (16,17,18). Phys. Chem. Chem. Phys. 14 (42), 14567–14572.

Fuchs, S., Schumann, D., Williams-Jones, A.E., Vali, H., 2015. The growth and concentration of uranium and titanium minerals in hydrocarbons of the Carbon Leader Reef, Witwatersrand Supergroup, South Africa. Chem. Geol. 393–394, 55–66.

Gao, F., Song, Y., Li, Z., Jiang, Z., Gao, Z., Zhang, X., Chen, L., Liu, Q., 2018. Pore characteristics and dominant controlling factors of overmature shales: a case study of the Wangyinpu and Guanyintang Formations in the Jiangxi Xiuwu Basin. Interpretation 6 (2), T393–T412.

Gregory, D.D., et al., 2017. Whole rock and discrete pyrite geochemistry as complementary tracers of ancient ocean chemistry: an example from the Neoproterozoic Doushantuo Formation, China. Geochim. Cosmochim. Acta 216, 201–220.

Guo, Q.J., Shields, G.A., Liu, C.Q., Strauss, H., Zhu, M.Y., Pi, D.H., Goldberg, T., Yang, X.L., 2007. Trace element chemostratigraphy of two Ediacaran-Cambrian successions in South China: implications for organosedimentary metal enrichment and silicification in the early Cambrian. Palaeogeogr. Palaeoclimatol. Palaeoecol. 254 (1–2), 194–216.

Hatch, J.R., Leventhal, J.S., 1992. Relationship between inferred redox potential of the depositional environment and geochemistry of the upper Pennsylvanian (Missourian) Stark shale Member of the Dennis Limestone, Wabaunsee Country, Kansas, USA. Chem. Geol. 99 (1–3), 65–82.

Henry, D.J., Guidott, C.V., 2002. Titanium in biotite from metapelitic rocks: temperature effects, crystal-chemical controls, and petrologic applications. Am. Mineral. 87 (4), 375–382.

Iliev, M.N., Hadjiev, V.G., Litvinchuk, A.P., 2013. Raman and infrared spectra of brookite (TiO_2): experiment and theory. Vib. Spectrosc. 64, 148–152.

Jiang, S.Y., Chen, Y.Q., Ling, H.F., Yang, J.H., Feng, H.Z., Ni, P., 2006. Trace-and rare-earth element geochemistry and Pb–Pb dating of black shales and intercalated Ni–Mo–PGE–Au sulfide ores in lower Cambrian strata, Yangtze Platform, South China. Mineral. Deposita 41 (5), 453–467.

Jin, C.S., Li, C., Algeo, T.J., O'Connell, B., Cheng, M., Shi, W., Shen, J., Planavsky, N.J., 2018. Highly heterogeneous “poikiloredox” conditions in the early Ediacaran Yangtze Sea. Precambrian Res. 311, 157–166.

Jones, B., Manning, D.A.C., 1994. Comparison of geochemical indexes used for the interpretation of palaeoredox conditions in ancient mudstones. Chem. Geol. 111 (1–4), 111–129.

Khan, H., Berk, D., 2014. Synthesis, physicochemical properties and visible light photocatalytic studies of molybdenum, iron and vanadium doped titanium dioxide. React. Kinet. Mech. Catal. 111 (1), 393–414.

Kristensen, E., 2000. Organic matter diagenesis at the oxic/anoxic interface in coastal marine sediments, with emphasis on the role of burrowing animals. Hydrobiologia 426 (1–3), 1–24.

Li, H., Zhao, G.L., Chen, Z.J., Han, G.R., Song, B., 2010. Low temperature synthesis of visible light-driven vanadium doped titania photocatalyst. J. Colloid Interface Sci. 344 (2), 247–250.

Ling, H.F., Burton, K.W., ONions, R.K., Kamber, B.S., von Blanckenburg, F., Gibb, A.J., Hein, J.R., 1997. Evolution of Nd and Pb isotopes in Central Pacific seawater from ferromanganese crusts. Earth Planet. Sci. Lett. 146 (1–2), 1–12.

Liu, Z.R.R., Zhou, M.F., 2017. Meishucun phosphorite succession (SW China) records redox changes of the early Cambrian ocean. Geol. Soc. Am. Bull. 129 (11 – 12), 1554–1567.

Lo Monaco, S., Lopez, L., Rojas, H., Garcia, D., Premovic, P., Briceno, H., 2002. Distribution of major and trace elements in La Luna formation, southwestern Venezuelan basin. Org. Geochem. 33 (12), 1593–1608.

Mandal, P.C., Goto, M., Sasaki, M., 2014. Removal of nickel and vanadium from heavy oils using supercritical water. J. Jpn. Pet. Inst. 57 (1), 18–28.

Parnell, J., 2004. Titanium mobilization by hydrocarbon fluids related to sill intrusion in a sedimentary sequence, Scotland. Ore Geol. Rev. 24 (1–2), 155–167.

Qi, L., Hu, J., Gregoire, D.C., 2000. Determination of trace elements in granites by inductively coupled plasma mass spectrometry. Talanta 51 (3), 507–513.

Schulz, H.-M., Wirth, R., Schreiber, A., 2016. Nano-crystal formation of TiO2 polymorphs brookite and anatase due to organic—inorganic rock–fluid interactions. J. Sediment. Res. 86 (2), 59–72.

Skrabal, S.A., 2006. Dissolved titanium distributions in the Mid-Atlantic Bight. Mar. Chem. 102 (3–4), 218–229.

de Souza, R.M., Meliande, A.L.S., da Silveira, C.L.P., Aucelio, R.Q., 2006. Determination of Mo, Zn, Cd, Ti, NiVFe, Mn, Cr and Co in crude oil using inductively coupled plasma optical emission spectrometry and sample introduction as detergentless microemulsions. Microchem. J. 82 (2), 137–141.

Steiner, M., Wallis, E., Erdtmann, B.D., Zhao, Y.L., Yang, R.D., 2001. Submarine-hydrothermal exhalative ore layers in black shales from South China and associated fossils - insights into a Lower Cambrian facies and bio-evolution. Palaeogeogr. Palaeoclimatol. Palaeoecol. 169 (3–4), 165–191.

Tachikawa, K., Athias, V., Jeandel, C., 2003. Neodymium budget in the modern ocean and paleo-oceanographic implications. J. Geophys. Res. Oceans 108 (C8), 3254.

Tribovillard, N., Algeo, T.J., Lyons, T., Riboulleau, A., 2006. Trace metals as paleoredox and paleoproductivity proxies: an update. Chem. Geol. 232 (1–2), 12–32.

Van Den Berg, C.M.G., Boussemart, M., Yokoi, K., Prartono, T., Campos, M.L.A.M., 1994. Speciation of aluminum, chromium and titanium in the NW Mediterranean. Mar. Chem. 45 (4), 267–282.

Wen, H.J., Carignan, J., Zhang, Y.X., Fan, H.F., Cloquet, C., Liu, S.R., 2011. Molybdenum isotopic records across the Precambrian-Cambrian boundary. Geology 39 (8), 775–778.

Wen, H.J., Fan, H.F., Zhang, Y.X., Cloquet, C., Carignan, J., 2015. Reconstruction of early Cambrian ocean chemistry from Mo isotopes. Geochim. Cosmochim. Acta 164, 1–16.

Xiong, Q., Zheng, J., Griffin, W.L., O'Reilly, S.Y., Zhao, J., 2011. Zircons in the Shenglikou ultrahigh-pressure garnet peridotite massif and its country rocks from the North Qaidam terrane (western China): Meso-Neoproterozoic crust–mantle coupling and early Paleozoic convergent plate-margin processes. Precambrian Res. 187 (1), 33–57.

Xu, L.G., Lehmann, B., Mao, J.W., Nagler, T.F., Neubert, N., Bottcher, M.E., Escher, P., 2012. Mo isotope and trace element patterns of Lower Cambrian black shales in South China: multi-proxy constraints on the paleoenvironment. Chem. Geol. 318, 45–59.

Yang, K., Lin, D.H., Xing, B.S., 2009. Interactions of humic acid with nanosized inorganic oxides. Langmuir 25 (6), 3571–3576.

Young, G.M., Nesbitt, H.W., 1998. Processes controlling the distribution of Ti and Al in weathering profiles, siliciclastic sediments and sedimentary rocks. J. Sediment. Res. 68 (3), 448–455.

Yu, R.Q., Wang, W.X., 2004. Biological uptake of Cd, Se(IV) and Zn by *Chlamydomonas reinhardtii* in response to different phosphate and nitrate additions. Aquat. Microb. Ecol. 35 (2), 163–173.

Zhang, H.Z., Banfield, J.F., 2014. Structural characteristics and mechanical and thermodynamic properties of nanocrystalline TiO_2. Chem. Rev. 114 (19), 9613–9644.

Zhang, H., Sun, M., Lu, F., Zhou, X., Zhou, M., Liu, Y., Zhang, G., 2001. Moderately depleted lithospheric mantle underneath the Yangtze Block: evidence from a garnet lherzolite xenolith in the Dahongshan kimberlite. Geochem. J. 35, 315–331.

Zhang, J.P., Fan, T.L., Zhang, Y.D., Lash, G.G., Li, Y.F., Wu, Y., 2017a. Heterogenous oceanic redox conditions through the Ediacaran-Cambrian boundary limited the metazoan zonation. Sci. Rep. 7 (1), 8850.

Zhang, Y., He, Z., Jiang, S., Gao, B., Liu, Z., Han, B., Wang, H., 2017b. Marine redox stratification during the early Cambrian (ca. 529–509 Ma) and its control on the development of organic-rich shales in Yangtze Platform. Geochem. Geophys. Geosyst. 18 (6), 2354–2369.